Cool Core Clusters in the Magneticum Pathfinder Simulation

Bachelor Thesis
at the Faculty of Physics
Ludwig–Maximilians–University Munich

Submitted by
Jennifer Hinz
born in Munich

Supervised by
PD Dr. Klaus Dolag

Munich, 22th of January 2018

Cool Core Cluster in der Magneticum Pathfinder Simulation

Bachelorarbeit
an der Fakultät für Physik
der Ludwig–Maximilians–Universität München

vorgelegt von
Jennifer Hinz
geboren in München

betreut von
PD Dr. Klaus Dolag

München, den 22.01.2018

Contents

1 Introduction: Cosmology and Galaxy Clusters

Cosmology deals with the universe as a whole. It investigates the origin of our universe and the evolution of time and space which is strongly correlated to the formation of structure and matter. The basic assumption from which cosmological theories are derived is the cosmological principle. It states that the universe is isotropic and homogeneous which simply means that no point in the universe is special and that on large scales the structure properties are nearly the same in every direction. [Schneider, 2008]
The two most important and fundamental discoveries of the last century concerning cosmology are the expansion of the universe and the cosmic microwave background (CMB). Measurements of the velocities of distant objects reveal that nearly all of these objects are drifting apart from us. Applying the cosmological principle, this means that everything in the universe is moving away from each other unless it is bound by gravitational interaction. The discovery of the cosmic microwave background on the other hand gives further evidence for the isotropy of the universe. This CMB with a temperature of 2.7 K is detected homogenously distributed over the entire sky and shows only very small anisotropies in its spectrum. [Boerner, 1995]
Using Einstein's general theory of relativity, a cosmological standard model can be derived that includes explanations for the two presented discoveries. In this model, the universe starts from a point of singularity with infinitely high temperatures densities and expansion rates, the so-called big bang. The real physical description of the evolution of the universe can only start at a fraction of a second of the age (10^{-43} s) of the universe. From this point on, the universe is increasing with definable expansion rates. After a short epoch of the formation of quarks, protons, neutrons and electrons, a longer photon dominated period follows. The universe is still very hot and dense, thus all electrons are free and no bound atoms exist. During this time, photons scatter frequently with the free electrons hence at that time the universe is non-transparent. Because of the expansion of the universe, the temperatures and densities of the particles begin to drop to lower values and finally reach a threshold at which the electrons "recombine" with the nuclei. The frequent photon scatter with electrons is stopped and the universe becomes transparent. The cosmic micro-wave background is a "freeze" of this state of recombination at which the universe gets matter dominated. Therefore, it describes the density distribution of particles at the earliest state of transparency. The observed anisotropies reflect small fluctuations in the density which lead to the further formation of structure in the universe. [Boerner, 1995]
The initially small density inhomogeneities grow with time as gravitational forces drag on the particles. Over-dense regions become denser whereas under-dense regions decrease

more in density, an effect called gravitational instability. In this context, the hierarchical structure model is introduced. It is based on the assumption that the majority of matter in the universe is dominated by cold dark matter (CDM) that only interacts gravitationally. Thus, the evolution of structure formation is driven by the CDM particles. The collapse of the dark matter (DM) into over-denser regions leads to a build-up of small DM haloes. The baryonic matter follows the DM haloes. As time goes on, the haloes start to grow and collapse further because of accretions and mergers of smaller objects. The halo potential deepens and thus the temperatures or respectively velocities of the matter inside increase. The hot matter builds up a pressure which counteracts the gravitational collapse and slows it down. The merger events become less and the gravitational potential and pressure equilibrate. This process is called virialization. It continues until the virial equilibrium ($\langle U \rangle = -2\langle K \rangle$) is reached. The virialized clusters contain many galaxies that are remains of the mergers of the DM haloes. If the clusters are supposed to form only because of the gravitational forces, they should behave self-similar. This means that the clusters were simply scaled versions of each other. On the contrary, if it is necessary to also consider more complex physics, observations should reveal discrepancies in the properties of clusters. In summary, it can be said that the properties of clusters contain a lot information that is useful to check cosmological models and structure formation theories. [Kravtsov and Borgani, 2012]
One main problem of cosmology is that only the one universe exists, from which "probes" can be taken and investigated. This lack of more possibilities to check the physics of the universe demonstrates the importance of numerical cosmological simulations. Only such simulations can help to set up universes that can reveal what physical effects are negligible and which ones are highly important during the process of structure formation. This requires that the simulations reproduce the observed physical properties of clusters and other structures correctly. Thus, it is a steady effort to improve and test existing simulations.
In this Bachelor Thesis, specific physical properties of the intra-cluster medium (ICM) of galaxy clusters that were simulated in the *Magneticum Pathfinder* simulations are compared to observational results. The outcome should give a measure for how well the simulation reproduces these physical processes. For this purpose, the thesis is subdivided into two main parts. The first part gives an approach on the theoretical foundations that are needed to conduct the examination. The second part then focuses on the study of the simulated cluster sample and the comparison with observations. The last chapter summarizes the results and provides a short prospect on further investigations that could be done.

2 Theoretical Approach on the Intra-Cluster Medium, Cooling Flows and Cool Core Cluster

In this chapter a summary about the properties of the intra-cluster medium (ICM) is provided. Therefore, it is divided into two main parts. The first section, Sect. 2.1, gives a detailed overview of the basic physics of the ICM. This includes models and theories that try to explain the observed characteristics of the ICM, its mass density distribution along the cluster and its origin. Furthermore, a full theory about the evolution of the ICM could be developed, the so-called Cooling Flow (CF) model. It predicts that clusters can be segregated into two kinds using their ICM properties. The first kind has cooling times shorter than the cluster age and for this reason develops a cool cluster core. These clusters are called Cool Core (CC) clusters. The other state describes clusters whose cooling times exceed the age of the cluster. These ones do not show cool cores and thus are named Non-Cool Core (NCC) clusters. The second section, Sect. 2.2, focuses on how clusters can be assigned to one state and what physical processes are responsible for the different properties of the cluster cores. Moreover, the distribution of CC and NCC clusters in observations and simulations is presented to give an impression of how important it is to understand the underlying physics of CC and NCC clusters.
Throughout this thesis, several abbreviations will be used which are summarized in Table 2.1.

Table 2.1: Overview of all abbreviations used throughout this thesis

Abbreviation	**Explanation**
CMB	Cosmic Microwave Background
CDM	Cold Dark Matter
DM	Dark Matter
ICM	Intra-Cluster Medium
CF	Cooling Flow
SZ	Sunyaev-Zel'dovich
cD	Central Dominant
CC	Cool Core
NCC	Non-Cool Core Cluster
T-M	Temperature-Mass

2.1 Intra Cluster Medium (ICM)

In 1970, the first mission to search the entire sky for extended X-ray sources was launched. The so-called *Uhuru* satellite found primary evidence of high X-ray luminosities that were radiated from massive galaxy clusters. Following observations including the *EINSTEIN* survey and the *Ariel 5* satellite confirmed and amplified this discovery. High-mass as well as low-mass clusters and groups reveal intense and large spatially extended X-ray emission ($200 - 3000\ kpc$) with luminosities of $L_X \approx 10^{43} - 10^{45}\ erg/s$.
The most crucial point for further investigations, is the identification of the source that is emitting these high X-ray luminosities. In the context of galaxy clusters, only two kinds of emission mechanisms are possible. The observed X-ray emission can either originate from a diffuse hot plasma or from a compact X-ray source such as an AGN or stellar X-ray binary. The large extension of the emission and the fact that the emission is not variable over the observed timescales rules out any kind of compact source. Thus, the origin of the high X-ray luminosities can be traced down to the emission from a hot diffuse plasma. This hot plasma is distributed within the entire cluster and is therefore called intra-cluster medium (ICM). [Sarazin, 2009], [Schneider, 2008]
In this section, several theories concerning the main physics and evolution of the ICM are introduced. Sect. 2.1.1 gives an overview of some physical properties of the ICM. In Sect. 2.1.2 the most simple physical model is used to derive the mass and density distributions of the ICM. Based on the knowledge about cluster evolution, Sect. 2.1.3 points out several models that explain the origin of the temperature and abundance of the ICM. Then, in Sect. 2.1.4, another theory is introduced that could describe the evolution of the ICM over time. Finally, problems and criticism of this theory are presented in Sect. 2.1.5.

2.1.1 Properties of the ICM

As stated above, the space inside a cluster is filled with hot diffuse gas that emits strong X-ray radiation. One key issue to derive the physical properties of this plasma, is the identification of the main emission mechanism that is responsible for the high X-ray luminosities. This can easily be done by an analysis of the X-ray spectra from observations. In general, the spectra can be divided into continuous spectra and line emission spectra from which different physical properties can be deduced.
The continuous spectra can be fitted with functions that are obtained from the physical models of different emission mechanisms. For example, spectra from a thermal bremsstrahlung emission have an exponential dependency on the photon frequency whereas the emission from inverse Compton scattering is proportional to a power-law of frequency. The best fits on the X-ray cluster spectra are provided by exponential functions that belong to thermal bremsstrahlung emission. This radiation, also called free-free emission, is emitted if an electron gets accelerated in the Coloumb field of atomic nuclei. Accelerated charged particles emit electro-magnetic dipole radiation and thus, the electron looses energy. This slows down the electron which is why the emission mechanism is called thermal bremsstrahlung. The spectral emissivity for thermal bremsstrahlung that is defined as the emitted energy

per unit time, frequency and volume, is given by the following equation (see e.g. [Schneider, 2008]):

$$\varepsilon_\nu^{ff} = \frac{32\pi Z^2 e^6 n_e n_i}{3m_e c^3}\sqrt{\frac{2\pi}{3k_B T m_e}}\exp(-h\nu/k_B T)\ g_{ff}(T,\nu), \tag{2.1}$$

in which Z is the ion charge, n_e is the electron number density, n_i is the ion number density and g_ν^{ff} is the Gaunt-factor. It gives a correction for quantum-mechanical effects and can be approximated as $g_\nu^{ff} \approx \frac{3}{\sqrt{\pi}}\ln\left(\frac{9k_B T}{4h\nu}\right)$. Integrating this equation over all frequencies and assuming that the gas mainly consists of hydrogen ($n_e \approx n_i$), gives the entire emissivity which is the emitted energy per unit time and volume (see e.g. [Schneider, 2008]):

$$\varepsilon^{ff} = \int_0^\infty \varepsilon_\nu^{ff}\ d\nu \approx 3.0\cdot 10^{-27}\sqrt{\frac{T}{1\ K}}\left(\frac{n_e}{1\ cm^{-3}}\right)^2 erg\ cm^{-3}\ s^{-1}. \tag{2.2}$$

With regard to Eq. (2.1), the X-ray spectra of thermal bremsstrahlung have to be proportinal to an exponential of the photon frequency ($I_\nu \propto \exp(-h\nu/k_B T_{gas})$). Therefore, if a fit of this is performed on X-ray spectra, the gas temperature of the hot diffuse plasma can be derived. An example of this is shown in Fig. 2.1. In this case, a temperature of 7.6 keV was determined by the thermal bremsstrahlung fit. In general, gas temperatures in the range of $2\cdot 10^7 - 2\cdot 10^8\ K$ are obtained from fits on the spectra of clusters. [Sarazin, 2009], [Schneider, 2008]

Emission line spectra can further confirm that the thermal bremsstrahlung is the correct emission mechanism related to the ICM. In a hot plasma, free electrons, that are accelerated by the atomic nucleii, can scatter with electrons that are still bound to the nucleii. This scatter excites the electron to a higher energy level or even frees it. Subsequently, another electron from a higher energy level is deexcited and emits a characteristic amount of energy that can be identified in the spectrum as line emission. The most significant line emission from thermal bremsstrahlung is the 7 keV iron line that is also found in the spectrum of Fig. 2.1. The cooler the gas, the more line emissions are detected e.g. lines from heavier elements such as C, N, O, Ne, Mg and Ca. Every line emission that is identified this way, gives an additional information on the abundance of the hot ICM. Generally it can be said that for the ICM of clusters a primoridal distribution of hydrogen and helium is assumed that is enriched by small fractions of metals with higher atomic numbers. [Sarazin, 2009], [Schneider, 2008]

To summarize, the main result from analysing the X-ray spectra of galaxy clusters is that the dominant emission mechanism for X-ray radiation of clusters is thermal bremsstrahlung. Fits on the continuous spectra reveal gas temperatures of the clusters whereas investigations of the line emission spectra provide information on the abundances of the ICM.

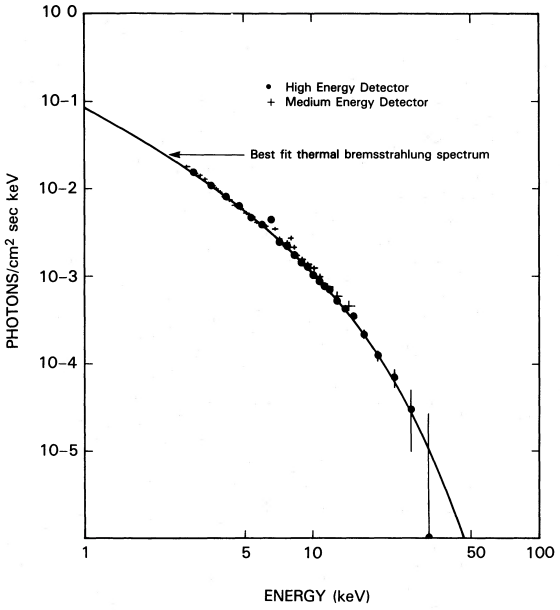

Figure 2.1: Composite HEAO 1 A-2 spectrum with data from medium- and high-energy detectors, showing the number flux of photons per $cm^2 - sec - keV$ versus the photon energy in keV. The best-fitting isothermal bremsstrahlung spectrum is plotted with a temperature of 7.6 keV. The figure is taken from [Henriksen and Mushotzky, 1986].

2.1.2 Hydrostatic Model of the ICM

Another important point when considering the hot thermal ICM, is its mass distribution along clusters. In this section, at first, the general mass distribution of isothermal and hydrostatically equilibrated matter is derived. For this model, the sort of matter that follow the obtained distribution is not specified, it could be dark matter or even galaxies. Afterwards, a transfer to the special case of ICM gas is conducted.
The isothermal model takes two basic assumptions. The first one is that the temperature distribution is supposed to be spatially constant at a temperature T. The second one states that the particles are assumed to be thermalized, meaning their velocity distribution follows a Maxwell distribution. Following these conditions, an approximation formula for the mass density distribution can be derived. Therefore, one starts with an hydrostatic equilibrium where the gravitational force is compensated by the pressure of the matter. [Schneider, 2008]

$$\nabla P = -\rho \nabla \Phi, \tag{2.3}$$

with P being the pressure of the particles, ρ referring to the particle density and Φ being the gravitational potential. This equation is simplified by postulating a spherically symmetric case and thus introducing spherical coordinates that only depend on the radius r [Schneider,

2008]:

$$\frac{dP}{dr} = -\rho\frac{d\Phi}{dr} = -\frac{GM(r)}{r^2}. \tag{2.4}$$

Differentiating Eq. (2.4) with respect to r and following the transformations, which can be reviewed in Appendix A.1, results in [Schneider, 2008]:

$$\frac{d}{dr}\left(\frac{r^2}{\rho}\frac{dP}{dr}\right) + 4\pi G r^2 \rho = 0. \tag{2.5}$$

To insert an expression for pressure, the thermodynamical equation of state is used [Schneider, 2008]:

$$P = nk_BT = \frac{\rho}{\langle m\rangle}k_BT, \tag{2.6}$$

with n being the number density, T referring to the temperature and $\langle m\rangle$ being the mean particle mass. The temperature of a system is a direct outcome of the velocities of the particles in the system. Thus, the correlation of temperature and velocity dispersion can be used to express the pressure in depencence of the velocity dispersion [Schneider, 2008]:

$$\frac{3}{2}k_BT = \frac{\langle m\rangle}{2}\langle v^2\rangle. \tag{2.7}$$

where $\langle v^2\rangle$ is the mean squared velocity of particles in a resting system. This quantity is related to the one dimensional velocity dispersion σ_v^2 that can be measured more easily in most cases. A velocity distribution that follows an isotropic Maxwell distribution has the same velocity dispersion in all three dimensions. The mean squared velocity in this case is the sum of all three one-dimensional velocity dispersions [Schneider, 2008]:

$$\begin{aligned}\langle v^2\rangle &= \sigma_x^2 + \sigma_y^2 + \sigma_z^2,\\ \sigma_v^2 &= \frac{\langle v^2\rangle}{3}.\end{aligned} \tag{2.8}$$

Using Eq. (2.7) and (2.8), a new expression for the derivative of the pressure can be found [Schneider, 2008]:

$$\frac{dP}{dr} = \frac{k_BT}{\langle m\rangle}\frac{d\rho}{dr} = \frac{\langle v^2\rangle}{3}\frac{d\rho}{dr} = \sigma_v^2\frac{d\rho}{dr}. \tag{2.9}$$

Finally, Eq. (2.5) and (2.9) lead to a differential equation defining the general radial mass density distribution [Schneider, 2008]:

$$\frac{d}{dr}\left(\frac{\sigma_v^2 r^2}{\rho}\frac{d\rho}{dr}\right) + 4\pi G r^2\rho = 0. \tag{2.10}$$

To find physically reasonable solutions for this equation, boundary conditions need to be set. $\rho(0) = \rho_0$ and $\frac{d\rho}{dr}|_{r=0} = 0$ are fixed to ensure a density profile that is flat at the center. Additionally, the velocity distribution needs to be cut to obtain finite total masses. With these adaptions, also called King models, an analytical approximation formula can be given [Schneider, 2008]:

$$\rho(r) = \rho_0 \left[1 + \left(\frac{r}{r_c}\right)^2\right]^{-3/2}, \tag{2.11}$$

with $\rho_0 = \frac{9\sigma_v^2}{4\pi G r_c^2}$ being the central mass density and r_c referring to the core radius which is defined as the radius at which the projected density has dropped to half the value of the central density. [Schneider, 2008]
After having derived a general mass density distribution, in the following, the mass density distribution of ICM gas particles is deduced. For this purpose, a short estimation is given to prove that the assumption of a hydrostatic equilibrium is fulfilled. A measure for this is provided by the speed of sound. This quantity describes how long a sound wave would need to cross the entire cluster. Thus, it can predict whether a pressure imbalance that existed at the beginning of structure formation could have equilibrated until today. In other words, the time a sound wave would need to cross the entire cluster has to be shorter than the age of the cluster [Schneider, 2008]. The speed of sound in thermodynamics is defined as:

$$c_s = \sqrt{\left(\frac{\partial P_g}{\partial \rho_g}\right)_S}, \tag{2.12}$$

with P_g being the pressure and ρ_g being the density of the gas particles. In an idealized approach, the gas of the ICM can be assumed as an ideal gas. Moreover, it is already known, that this gas mainly consists of hydrogen and a small fraction of heavier elements. Thus, the equation of state for this case is:

$$P_g = n_{e,g} k_B T_g = \frac{\rho_g k_B T_g}{\mu m_p}, \tag{2.13}$$

where m_p is the proton mass and μ is the mean molecular weight in proton masses. Using the above mentioned abundance, the mean molecular weight is approximately $\mu \approx 0.63$. The expression of Eq. (2.13) can be inserted into Eq. (2.12) [Schneider, 2008]:

$$c_s = \sqrt{\left(\frac{\partial P_g}{\partial \rho_g}\right)_S} = \sqrt{\frac{\partial\left(\frac{\rho_g k_B T_g}{\mu m_p}\right)}{\partial \rho_g}} = \sqrt{\frac{k_B T_g}{\mu m_p}} \approx 1000 \frac{km}{s}, \tag{2.14}$$

where typical gas temperatures of $T_g \approx 10^7 - 10^8\ K$ are assumed to estimate the range of velocities. Using the mean extension of a cluster that is about $r \approx 1.5\ Mpc$, the time scale

for the expansion of a sound wave over the entire cluster can be derived [Schneider, 2008]:

$$t_s = \frac{2 \cdot R_{cluster}}{c_s} \approx 10^9 \ yr. \tag{2.15}$$

This time is short in comparison to the age of the cluster ($t_{age} \approx H_0^{-1} \approx 1.44 \cdot 10^{10} \ yr$). Thus, a hydrostatic equilibrium as given in Eq. (2.3) can be assumed for the gas mass density [Schneider, 2008]:

$$\nabla P_g = -\rho_g \nabla \Phi. \tag{2.16}$$

Following, Eq. (2.4), a transformation into spherical coordinates can be done [Schneider, 2008]:

$$\frac{1}{\rho_g}\frac{dP_g}{dr} = -\frac{d\Phi}{dr} = -\frac{GM(r)}{r^2}, \tag{2.17}$$

where the mass $M(r)$ refers to the total mass of the cluster (not only the gas mass) because the entire mass of the cluster determines the gravitational potential. Inserting Eq. (2.13) into Eq. (2.17) and transforming the derivatives, gives the total mass distribution profile of a cluster [Schneider, 2008]:

$$M(r) = -\frac{k_B T_g r^2}{G\mu m_p}\left(\frac{d\ln(\rho_g)}{dr} + \frac{d\ln(T_g)}{dr}\right). \tag{2.18}$$

With this equation, $M(r)$ can be immediately deduced if the density distribution and temperature distribution of a cluster are known. However, the problem remains of how to obtain this density and temperature distribution. Therefore, the previously stated isothermal model is applied to Eq. (2.18). This means, the temperature distribution of the cluster is supposed to be constant $T = T_g$ and the last term of the mass distribution expression drops out [Schneider, 2008]:

$$\frac{d\ln\rho_g}{dr} = -\frac{\mu m_p}{k_B T_g}\frac{GM}{r}. \tag{2.19}$$

A comparison of Eq. (2.10) and Eq. (2.19) reveals that the gas mass density distribution follows the general mass density distribution according to a power law [Schneider, 2008]:

$$\rho_g(r) \propto [\rho(r)]^\beta, \tag{2.20}$$

with $\beta = \frac{\mu m_p \sigma_v^2}{k_B T_g}$. At last, the King model can also be applied to this distribution which results in [Schneider, 2008]:

$$\rho_g(r) = \rho_{g0}\left[1 + \left(\frac{r}{r_c}\right)^2\right]^{-3\beta/2}, \tag{2.21}$$

with $\rho_{g,0} = \rho_0^{\beta}$. Thereby, a formula is found that describes the radial mass density distribution of the ICM particles in a cluster.
Still, this distribution cannot be obtained directly from observations. The only quantity that can be measured in a direct way is the projected X-ray surface brightness profile of a cluster. This surface brightness profile is related to the deprojected emissivity of Eq. (2.1) following [Schneider, 2008]:

$$I_\nu(R) = 2\int_R^\infty dr \frac{\varepsilon_\nu(r) r}{\sqrt{r^2 - R^2}}, \tag{2.22}$$

where R is the measured projected radius and r is the deprojected radius. As stated in Eq. (2.1), the emissivity is proportional to the squared electron number density (assuming that the gas consists mainly of hydrogen $n_e \approx n_i$). This depencency makes it possible to fit the X-ray surface brightness I_ν to a King model in the following way [Schneider, 2008]:

$$I(R) = I_0 \left[1 + \left(\frac{R}{r_c}\right)^2\right]^{-3\beta+1/2}. \tag{2.23}$$

The derived values from the fits on the surface brightness profiles can be used to determine the mass density distributions of clusters. Using this method, the electron number densities of the ICM were found to lie within a range of $n_e \approx 10^{-4} - 10^{-2}\ cm^{-3}$ [Fabian, 1994]. [Schneider, 2008]

2.1.3 Origin of the ICM

After the study of the main properties of the ICM, another key point in the understanding of the ICM is the identification of the processes that heated and distributed it within the cluster and enriched it with the observed abundances. Different theories are necessary to give an holistic explanation. The hierarchical structure formation model provides the solution for how the ICM was heated and distributed whereas an early ejection model describes how the ICM was enriched by heavier elements.
In the hierarchical structure formation model, the primordial gas, that consists of hydrogen and helium, collapses following the gravitational dark matter collapse. Diffuse and relatively cold gas is accreted on to the cluster and encounters the heated gas at the inner region. The gas goes through an accretion shock which converts the kinetic energy of the gas into thermal energy. Thus, the gas is heated. The higher temperature of the gas slows down the gravitational collapse and the gas starts to virialize. As more and more gas is accreted and heated over time, the accretion shock moves outwards. Clusters at $z = 0$, for example, reveal accretion shocks at about two times their virial radius. Although the gas is heated by the accretion shocks, they alone are not sufficient to reach the observed temperatures. Another kind of shock is necessary to reach temperatures of about $10^8\ K$. Such shocks develop if substructures merge at the inner region of a cluster that was already heated. The shock of the collision propagates through the dense hot gas and heats it to

the observed levels. [Dolag et al., 2008], [Ha et al., 2017]
The only known mechanism for the yield of heavier elements is the processing of gas in stars. The question to answer in this context is how the ejected material of gas could be distributed in the ICM of galaxy clusters. In the past few years, a theory in this field made huge progress and was confirmed by simulations and observations. Observations such as the ones performed by [Simionescu et al., 2015] revealed that the chemical enrichment of the ICM extents out to the cluster outskirts. Such a distribution of the ejecta of stars can only be explained by an enrichment that took place at early times ($z > 2$) which was confirmed by several simulations ([Biffi et al., 2017], [Fabjan et al.,]). During the phase of structure formation at these early times, early star populations formed within the galaxies that were not yet bound to the proto-cluster. These stars ejected heavier elements in a combination of supernovae and winds which formed large hot bubbles including magneto-hydrodynamical motions and shocks. If these bubbles were very high energetic they could spread beyond their host galaxy and create a kind of "super-wind" that enriched the ICM. Furthermore, also AGN feedback within these early galaxies created bubbles that transported heavier elements out the ICM. [Dolag et al., 2008]
The combination of these theories presents a comprehensive explanation for the origin of the ICM. Simulations and observations have confirmed these models so that they are widely accepted today.

2.1.4 Evolution of the ICM: The Classical Cooling Flow (CF) Model

Soon after the detection of the hot ICM filling the space in-between cluster galaxies, a new theory for the evolution of this gas was derived. As the gas continuously looses thermal energy due to thermal bremsstrahlung, there will be a final threshold at which the energy losses are no longer negligible. This threshold is set by the so called cooling time. To derive this quantity, two basic assumptions are made. The first one states that the gas emits a constant amount of energy within a certain time over very long periods. This constant loss of energy is given by the emissivity that was already introduced in Eq. (2.2). The second point is that the entity of the gas can only posses a specific amount of thermal energy due to its temperature $E_{gas,thermal} = \frac{3}{2} n k_B T$. The cooling time t_{cool} is then defined as the time the gas would need until all of its thermal energy is radiated away [Schneider, 2008]:

$$t_{cool} = \frac{E_{gas,thermal}}{\varepsilon^{ff}} \approx 8.5 \cdot 10^{10}\ yr \left(\frac{n_e}{10^{-3} cm{-}3}\right)^{-1} \left(\frac{T_g}{10^8 K}\right)^{1/2}. \tag{2.24}$$

If the cooling time is smaller than the age of the system $t_{cool} < t_{age}$, cooling effects due to the radiative losses become noticeable and the hydrostatic assumption is no longer correct. [Schneider, 2008], [Fabian, 1994]
The classical Cooling Flow (CF) model describes the impact of cooling on the ICM. If the gas is relaxed, which means if it has had enough time to create a hydrostatic equilibrium as described in Sect. 2.1.2, then the gas at the core region of the ICM has the highest density. The cooling time, as it is indirectly proportional to the electron density, is smallest in this

region. If the age of the system exceeds the cooling time of this inner region, efficient cooling takes place and the gas reduces its temperature because of the radiated thermal energy. Following this, the pressure, which depends on density and temperature for an ideal gas, is reduced and the hydrostatic equilibrium breaks down. The gravitational force does no longer have a strong counterpart and starts to drag the ICM particles towards the center. By this, the core region becomes more and more condensed, as the inflowing masses from outer regions push towards the center. The density in the inner core regions increases and starts to build a new counterpart to the gravitational pressure due to its increased gas pressure. A new hydrostatic equilibrium is set up with higher core density but lower temperature. As the denser core is now cooling even more efficiently, an accelerated cooling circle develops, in which the core cools down and condenses and a constant inflow of gas from outer regions takes place, a so-called CF. [Fabian, 1994], [Sarazin, 2009]
A quantity that is often used to determine the thermodynamical properties of the ICM is the entropy [Voit et al., 2005]. According to the second law of thermodynamics, the entropy increases in heating processes and decreases for cooling processes. As stated above, a CF develops if efficient cooling takes place. With the loss of energy which increases towards the center, the entropy of this core region has to decline with declining radius. Thus, the entropy is a good measure for how efficient the cooling in the central region of the cluster has been and if a CF has developed. In astrophysics, the astrophysical entropy

$$K = n_e^{-2/3} T \tag{2.25}$$

is used for such purposes. For a detailed derivation and the correlation between the astrophysical entropy K and the thermodynamical entropy S see Appendix A.2.
The first confirmations of the CF model were given by observations of several clusters. These clusters showed intense evidence for cooled regions at their center because they revealed strong central peaks in their X-ray surface brightness profiles. From these peaks, the mass deposition rates associated with the CFs can be estimated. Assuming that all emission comes from thermal bremsstrahlung and that work is done on the gas when it reaches the cooling regions, the mass deposition rate $\dot{M}$ can be linked to the luminosity of the cooling region L_{cool} [Fabian, 1994]:

$$\dot{M} = \frac{2\mu m}{5 k_B T_g} L_{cool} \tag{2.26}$$

Typical values for L_{cool} and T_g can be inserted to deduce the mass deposition rates that can be expected. This results into values of $\dot{M} = 100 - 1000\ M_\odot\ yr^{-1}$. Additional theories are necessary to explain what happens to this large amount of gas that gathers in the center. One option is that the gas could cool below temperatures at which it could get bound to the central galaxy. In fact, many clusters possess central dominant (cD) galaxies which are very bright. This gives indication that a large amount of the cooled gas condenses and starts to form stars causing the very high luminosities of these galaxies. [Fabian, 1994], [Sarazin, 2009]

2.1.5 The Cooling Flow (CF) Problem

Missions performing further X-ray observations such as *NEWTON*, *CHANDRA*, etc. made it possible to conduct measurements of brightness profiles, temperature profiles and abundances of clusters in more detail. Differing from expectations, these surveys revealed a much lower amount of cooled gas [Sanders et al., 2008], [Molendi and Pizzolato, 2001], a lower star formation rate [McNamara, 2004], [McNamara and OConnell, 1989] and lower abundances of CO and molecular gas [Edge, 2001] than predicted. Concerns about the classical CF model were also emphasized by the detection that the ICM at the center reached a kind of cooling floor, a threshould below which nearly no temperature and entropy cooled [Peterson et al., 2003]. Only very little X-ray emission from gas cooled below the virial temperature of the cluster could be found [Peterson et al., 2003] (The virial temperature in this case refers to the temperature a cluster has in virial equilibrium depending on its mass). Additionally, also the entropy of the gas at the inner regions seemed to reach a lower threshold at approximately $K_0 = 10keVcm^2$ [Donahue et al., 2006]. In summary, these discrepancies led to deep doubts in the classical CF model and encouraged the search for new models and possible solutions.
The most approved solution to the CF problem is that some kind of feedback mechanism has to offset the cooling. That is, cooling is reduced by a an energy input resulting from a sort of feedback. This feedback would keep the cool core of the clusters but could prevent the cluster core to form stars at the predicted rates and to cool below the observed thresholds. Many potential sources for such mechanisms have been offered in publications:

- Mechanical Feedback from central AGN [Churazov et al., 2005]
- Soundwaves and conduction [Ruszkowski et al., 2004]
- Turbulence and conduction [Dennis and Chandran, 2005]

Since the cooling floor is kept constant over long periods, there needs to be a source which constantly injects energy. Therefore among all the possibilities, an explanation tracing the inferred energy back to AGN feedback is most common. Simulations including AGN feedback showed promising results, reinforcing these assumptions [Ruszkowski and Begelman, 2002], [Dubois et al., 2011].

2.2 Cool Core and Non-Cool Core Clusters (CC and NCC)

The general validity and scope of the classical CF model was more and more critically examined. No new or additional theory provided solutions that were sufficient to explain or solve the problems. Connecting the terminology of CFs to an obviously not sufficient model, a new nomenclature for the observed characteristics was proposed. This nomenclature should rather concentrate on the observed quantites than on the physical properties. This way, the term could not be linked to a wrong or deficient theory. The main observational characteristic of clusters with CFs, is their bright central peak in Xray emission, indicating

a low temperature at the central region of the cluster because of strong cooling. Therefore the nomenclature Cool Core (CC) cluster was chosen. Clusters not showing any evidence of a cool core region henceforward were called Non-Cool Core (NCC) cluster. The renaming following this process was introduced by [Molendi and Pizzolato, 2001].
This section gives an introduction on how observations and simulations can be used on the one hand to further clarify the different properties of CC and NCC clusters and on the other hand to predict how the distribution of CC and NCC clusters develops. For this reason, the first section, Sect. 2.2.1, provides an overview of different criteria and threshold values that are used to classify CC and NCC clusters. Subsequently, Sect. 2.2.2 presents how CC and NCC clusters are distributed in different observation samples. Based on these results, Sect. 2.2.3 introduces several theories that try to explain the origin of the distribution. Finally, in Sect. 2.2.4 the importance of simulations in this context is pointed out.

2.2.1 CC and NCC Cluster Classification

Before the change in designation, CFs clusters were mainly identified by showing bright centered X-ray peaks or having high mass deposition rates. With the redefinition to the term CC clusters, also new parameters were introduced to classify the state of a cluster as CC or NCC. For many observations, the CC and NCC fractions of their samples were determined using different criteria (e.g. [Andrade-Santos et al., 2017], [Sanderson et al., 2006], [Hudson et al., 2009], [Vikhlinin et al., 2006]). Some of these criteria concentrate on identifying a cooling process while others keep focus on finding cooled regions [Hudson et al., 2009]. In the following, the most common parameters are introduced and thresholds to segregate CC and NCC clusters are given as presented by [Hudson et al., 2009]. [Hudson et al., 2009] provided a detailed observational study on a representative sample of 64 clusters from the HIFLUGCS cluster sample. The central region this paper is defined as $0.00 - 0.048\ r_{500}$. r_{500}, in this case, refers to the radius at which the density of the cluster has reached a value of 500 times the critical density. The following list gives an overview of the most important diagnostics that were introduced and investigated:

- The central surface brightness I_0 and the inner core radius r_c as presented in Eq. (2.23). The values of these two quantities are derived by fitting the King model profile to the observed X-ray surface brightness profiles. A convenient threshold for segregating CC and NCC clusters with the central surface brightness is $I_0 = 0.8 \cdot 10^{-6}\ photons\ cm^{-2}\ s^{-1}\ arcsec^{-2}$. For the inner core radius, the boundary is set at $r_{c,0} = 1.3 \cdot 10^{-2}\ r_{500}$.

- The central electron number density $n_{e,0}$ that can also be derived from the King model fit on the mass density distribution of Eq. (2.21). CC and NCC clusters are segregated best at a value of $n_{e,0} = 1.5 \cdot 10^{-2}\ cm^{-3}$.

- The central entropy K_0 that is calculated according to Eq. (2.25). [Hudson et al., 2009] sets a threshold value of $K_0 = 150\ keV\ cm^2$.

- The central cooling time. In this publication it is calculated differently as presented in Eq. (2.24. However, the boundary of $t_{cool,0} = 7.7\ Gyrs$ is suitable in both cases.
- The cooling radius that is set at the radius where the central cooling time reaches $t_{cool}(r_{cool}) = 7.7\ Gyr$. All clusters with cooling times above $7.7Gyr$ are assigned a cooling radius of $r_{cool} = 0$. CC and NCC clusters are separated at $r_{cool,0} = 0.043\ r_{500}$.
- The scaled classical mass deposition rate defined as $\dot{M}_{classical}(< r) = \frac{M_{gas}}{t_{cool}(r) - t_{cool}(0)}$. The partition value is $\frac{\dot{M}_{classical}}{M_{500}} = 0.5 \cdot 10^{14}\ yr^{-1}$.
- The central temperature drop $\frac{T_0}{T_{vir}}$. This quantity separates the sample best at $\frac{T_0}{T_{vir}} = 0.7$.
- The cuspiness α which is often used for clusters at high z. According to [Vikhlinin et al., 2006], it is defined as $\alpha = -\frac{d\log(n)}{d\log(r)}$ at $r = 0.04r_{500}$. The segregation value is $\alpha = 0.75$.
- Also, the concentration parameter C_{SB} can be used for clusters at high z. This quantity was introduced by [Santos et al., 2008] as $C_{SB} = \frac{I(r<40\ kpc)}{I(r<400\ kpc)}$ with $I(r < 40\ kpc)$ being the integrated surface bright within 40 kpc. This quantity sets a boundary at $C_{SB} = 0.75$.

[Hudson et al., 2009] identified the best parameters for the segregation of low-redshift CC and NCC clusters as the central cooling time and the central entropy. For high-redshift clusters, the cuspiness and concentration parameter are found to separate the samples best.

2.2.2 Distribution of CC and NCC Clusters from Observations

Using the parameters that were introduced in the previous section, the fractions of CC and NCC clusters in observations can be determined. For this purpose, convenient samples of observed clusters are necessary. Generally, two kinds of cluster surveys can be used to derive the properties that are needed to classify the state of a cluster. The most common method, which has been used for several decades, is X-ray flux-limited observations. In these surveys clusters and their characteristics are identified by their strong extended X-ray emissions. On the other hand, lately many detections and investigations of clusters have been conducted using the Sunyaev-Zel'dovich (SZ) effect. Cluster samples that are derived by using this effect are called SZ-samples. For an explanation of how the effect works, see Appendix A.3.
The CC fractions obtained from X-ray flux-limited samples can be strongly biased. CC clusters have high X-ray emissivities due to strong thermal bremsstrahlung at their centers and consequently are brighter than NCC clusters. Thus, CC clusters are more likely to be found in X-ray flux-limited surveys and the samples therefore suffer a selection bias (Malmquist bias). Recently, a detailed study of the CC fraction from clusters observed with the SZ effect and clusters detected in X-ray flux-limited survey revealed that the CC

fractions of X-ray selected clusters are overestimated by a factor of $2.1 - 2.7$ [Andrade-Santos et al., 2017]. This needs to be kept in mind when examining CC fractions.
Several results from X-ray surveys are presented in the following. [Andrade-Santos et al., 2017] found 54% of their 100 low-z clusters to be CC clusters regarding their central electron number density. However, [Hudson et al., 2009] determined that 72% of their 64 lower-z clusters were CC cluster according to the central cooling times. [Sanderson et al., 2006] used the central temperature drop of 20 X-ray selected clusters to determine a CC fraction of 45% in their sample.
Likewise, some outcomes from SZ observations can be cited. [Andrade-Santos et al., 2017] also investigated 164 clusters at low z. They identified only 40% of these clusters as CCs using the central electron number density. [Rossetti et al., 2017] determined the CC fraction of 189 clusters to be 29% according to the concentration parameter.
To use the advantages of X-ray observations but minimize the bias effects, a mixture of both kinds of surveys can be used to perform more detailed studies. For example, [McDonald et al., 2013] selected 83 clusters of an SZ survey and explored their cooling properties using their *Chandra* X-ray observation data. Their main result was that the CC fraction of clusters does not change with higher redshift. Therefore, they suggest that possibly AGN feedback could balance the cooling of clusters over long time-scales.
In summary, many different CC and NCC fractions for different values and surveys are found. It is always important to consider which criteria are used and what kind of cluster sample is selected if the fractions are compared. The only correlation that can be derived from all of these surveys is that CC and NCC cluster are more or less equally common with a slight trend to finding more NCC clusters.

2.2.3 The Origin of the Distribution of NCC and CC Clusters

The previous section showed that a nearly equal distribution of CC and NCC clusters among all clusters can be supposed. This means that neither CC nor NCC clusters are just special cases. Some fundamental physical difference in the gas properties of these clusters has to determine their state. To identify this difference, the origin for the distribution of CC and NCC clusters has to be identified. In the following, several theories are presented that try to explain the reason why CC and NCC clusters exist.
The original model, that is also chosen as an explanation in the CF model, describes the CC state as the natural state of clusters. Following the classical CF model, the ICM looses energy due to radiation until the age of the system exceeds the cooling time. Finally, cooling effects overweigh and lead to further and more rapid cooling and condensing of the core region. That is, a CC cluster develops. The cluster stays in this state until it gets disturbed by a merger event, a collision of two clusters. Evolving shock fronts heat and mix the ICM during the merger. The cool core region vanishes and the cluster changes its state, becoming a NCC cluster. After the merger event, the cluster slowly relaxes and begins to radiate in X-ray again. The procedure to forming a CC cluster restarts. To summarize, it is assumed, that CC and NCC clusters build up in cyclic evolution. Several recent observations and simulations also confirmed this theory such as [Sanderson et al.,

2006], [Rossetti and Molendi, 2010] and [Hahn et al., 2015].
Nevertheless, there is a controversy in literature about the origin of the CC and NCC cluster distribution. [McCarthy et al., 2004] presented that their simulations produced too high fractions of CC clusters although they included merger events. Because of this reproduction of too high CC fractions, called overcooling problem, [McCarthy et al., 2004] developed a new theory to give a proper explanation matching their findings. The so-called primordial model acts on the assumption of non gravitational pre-heating in early times such as galactic winds or strong AGN feedback. During this period, some clusters got heated above a level of 300 $keV\ cm^2$ and therefore simply could not cool until today. These clusters are nowadays identified as NCC cluster. CC cluster whereas were heated to lower levels and therefore could form cool cores. [McCarthy et al., 2004], [McCarthy et al., 2008]
Another model that also assigns the origin of the CC - NCC distribution to earlier times, predicts that only major mergers at an early epoch were strong enough to destroy young developing cool cores. Thus, if an early merger of clusters happened, this cluster would from then on be a NCC. If in early times only smaller mergers occured and a major merger took place at a later epoch, it could not destroy an existing cool core. With this assumption, CC clusters would not be more relaxed than NCC clusters. [Burns et al., 2008], [Henning et al., 2009], [Poole et al., 2008]
Favoring a model of cyclic evolution of CC and NCC clusters, some simulations assume that clusters change their states as CC and NCC cluster during their lifetime because of AGN activity and conduction. A cluster that starts at a CC state has a low heat conductivity and therefore strong cooling with strong CFs. The inflowing masses trigger the AGN which finally results in an AGN outburst. This heating due to strong AGN feedback increases the conductivity again and can change the state of the cluster to a NCC cluster. The cluster can then either remain in this NCC state if conductivitiy is preserved or a heat flux driven buoyancy instability can occur if the temperature drop towards the center is strong enough. This kind of instability limits or even terminates conduction towards the center and the cluster returns to a CC state. [Guo and Oh, 2009]
In summary, several theories have been developed that try to give an explanation on the origin of the CC NCC cluster distribution. Some models suppose the state of a cluster is set once in early times and remains the same over the entire life-time. Other positions prefer a cyclic evolution in which the state of a cluster can change over time.

2.2.4 CC and NCC Clusters in Numerical Simulations

Based on the results from observations as stated in Sect. 2.2.2, another interesting point regarding CC and NCC clusters is how well the observed fractions and thermodynamical properties of the ICM are reproduced by simulations. Cosmological simulations that try to reconstruct the formation of galaxy clusters are usually set up the follwing way. The initial conditions are given by an initial density field that shows only very small density fluctuations around the cosmic mean density. Two kinds of forces are introduced to exert on the matter that is set up in this initial condition. The hydrodynamical forces only act on

baryons while gravitational force exerts on dark matter particles and baryonic matter. The gravitational force can be calculated by using the grid-based particle mesh method (PM), the particle/particle/particle-mesh method (P^3M) or the gridless tree method. However, hydrodynamics are implemented as the gridless smoothed particle hydrodynamics method (SPH) or shock-capturing grid-based methods such as Smoothed Lagrangian Hydrodynamics (SLH) or Adaptive Moving Mesh. In addition, many other mechanisms such as radiative cooling processes, heat conduction and general AGN feedback have to be considered to ensure consistency with observations. [Kravtsov and Borgani, 2012]
Many early simulations failed to reproduce the observed CC and NCC fractions (e. g. [Kay et al., 2007], [Burns et al., 2008]). The main difficulty, in this context, was the correct reconstruction of the interaction between radiative cooling and the convenient heating mechanisms [Kravtsov and Borgani, 2012]. Different models of the origin of the CC and NCC distribution were tested in simulations to achieve a correct replication of CC and NCC clusters. The results thereof were quite contradictory. Some simulations confirmed the theories of cylcic evolution whereas others approved pre-heating models [McCarthy et al., 2008], [Burns et al., 2008], [Guo and Oh, 2009]. [Rasia et al., 2015] and [Barnes et al., 2017] recently presented two promising sets of simulations that reproduced CC fractions quite well. Many different and complex physical effects are implemented in their studies which makes their results more reliable than the ones from earlier simulations.
The aim of this bachelor thesis is to investigate the CC fraction and properties of CC and NCC clusters from a cluster sample of the *MAGNETICUM Pathfinder* simulation [Nagai and Dolag, prep]. These simulations consist of a set of cosmological hydrodynamical simulations which are based on the *P-GADGET 3* code by Volker Springel, a parallel cosmological Tree Particles-Mesh code with SPH implementation. Several physical extensions such as AGN feedback, black holes, thermal conduction, magnetic fields, cooling, star formation and winds have been added and implemented in order to further improve the code. The simulations start at high redshift and evolve up to $z = 0$. For several values of z during the run, snapshots are created that include all necessary data. The simulations use parameters from the ΛCDM model as presented by [Komatsu et al., 2011]. Therefore, the total matter density is $\Omega_0 = 0.272$, the cosmological constant is determined as $\Lambda_0 = 0.728$ and the Hubble constant is $H_0 = 70.4$.
For this study, simulation *Box2/hr* is chosen which expands over a range of 352 Mpc/h and comprises $2 \cdot 1583^3$ particles in high resolution. This results in a mass resolution of $6.9 \cdot 10^8$ $M_\odot/h$ for dark matter particles and $1.4 \cdot 10^8$ $M_\odot/h$ for gas particles. A softening of 3.75 kpc/h for dark matter and gas particles is chosen to avoid a divergence of forces if particles get too close to each other. For the following investiagtions, snapshot 136 from *Box2* is selected that corresponds to a low redshift of $z = 0.066$. Using this value, the results can be more easily compared to surveys of nearby clusters.

3 CC and NCC Clusters in the MAGNETICUM Simulation

This chapter provides a detailed analysis of CC and NCC clusters that can be found in the *Magneticum Pathfinder* simulation. As exemplified in the previous chapter, the properties of the hot ICM of clusters need to be investigated to classify clusters as CC or NCC clusters. Thus, the first section of this chapter, Sect. 3.1, gives a short overview on how the ICM of the simulated clusters is derived and what clusters from the simulation will be studied in the following. In Sect. 3.2 four parameters of the ones that were presented in Sect. 2.2.1 are selected and the cluster sample is studied for its CC and NCC states using these criteria. Sect. 3.3 further examines the difference of the thermal structure and thermodynamical properties of several clusters that were classified as CC or NCC clusters in Sect. 3.2. Finally, the last section, Sect. 3.4, investigates the correlation between the state of a cluster as CC or NCC, the relaxation morphology of a cluster and the scatter among the T-M scaling relation to make a first conjecture about the origin of the CC and NCC distribution.

3.1 Clusters and ICM in MAGNETICUM

The *Magneticum Pathfinder* simulation already differs between different types of particles. For example, dark matter particles only interact due to gravitational forces, whereas gas particles are also sensible to hydrodynamics. Several snapshots are produced while the simulation runs. Each of these outputs is taken at a different time (different redshift z) and includes all necessary information about the different particles such as positions, velocities and masses. [Springel, 2005]
The snapshots only contain indirect information about the structures that were built during the run. To clearly identify structures such as clusters or galaxies a special algorithm has to be run on the snapshot data. For this purpose, the Friends-of-Friends (FoF) - Algorithm is used. This kind of algorithm identifies groups of particles within a specific overdensity. Therefore, a linking length is defined which determines how dense the particles have to get to be identified as groups. If the distance of two particles to each other is smaller than this linking length, these particles are linked to another. If the distance of a third particle to one of these two particles is smaller than the linking length, this particle is also linked to them and so on. The groups of particles which are identified that way will from now on be referred to as haloes. [Springel et al., 2000], [Dolag et al., 2009]
As soon as these kind of parent haloes are identified, it is also necessary to find substruc-

tures within these haloes. Such substructures are defined as locally overdense, self-bound particle groups within a larger parent group. For this purpose, the *SUBFIND* routine is used which combines and improves several known algorithms and can even detect haloes within haloes. [Springel et al., 2000], [Dolag et al., 2009]
Using the review done by the *FoF* and *SubFind* algorithms, all particles of the simulation are then assigned to haloes or even to subhaloes. In observations, the extension of a cluster is limited to a certain radius at which the density of the cluster has reached a certain value of a reference density. Similar to this, in the simulation only gas particles that are located within a radius that is lower than r_{500}, the radius at which the density of the cluster is 500 times the critical density of the universe, are selected. Likewise, the gas particles of a subhalo can be gathered if only particles within the subhalo borders are taken. For the investigations done in this thesis, only ICM particles are of interest. For this reason, the ICM particles of each halo have to be selected from the snapshots. Therefore, at first all gas particles of a halo are selected. Then, the ISM particles are chosen by finding out which of them also belong to subhaloes. The ISM particles are subtracted from the gas particles in the following. This leaves only the ICM particles in the gas particle sample. To ensure that these are only particles of the hot diffuse ICM, in addition, star forming regions have to be excluded. The thresholds set therefore are gas temperatures above $2 \cdot 10^5 K$ and cold fraction rates below 0.001.
A large sample of 1199 haloes from the simulation is selected spanning a mass range from $1.44 \cdot 10^{15}\ M_\odot - 5.27 \cdot 10^{13}\ M_\odot$. The haloes are chosen according to the same mass criteria as presented in [Barnes et al., 2017] who published a census of CC cluster from the Illustris TNG simulation. Following [Barnes et al., 2017] the *MAGNETIUM* sample can also be subdivided into three mass samples which yield 121 high-mass haloes ($2.00 \cdot 10^{14}\ M_\odot - 1.44 \cdot 10^{15}\ M_\odot$), 407 intermediate-mass haloes ($9.00 \cdot 10^{13}\ M_\odot - 2.00 \cdot 10^{14}\ M_\odot$) and 671 low-mass haloes ($5.27 \cdot 10^{13}\ M_\odot - 9.00 \cdot 10^{13}\ M_\odot$). The *IllustrisTNG* simulation only comprises 370 clusters in total with 49 high-mass clusters, 139 intermediate-mass clusters and 191 low-mass clusters [Barnes et al., 2017].

3.2 Analysis of CC Parameters in MAGNETICUM

The following parameters are selected for an investigation of the CC fractions in Sect. 3.2.1, an analysis of the their correlation in Sect. 3.2.2 and to introduce a new parameter in Sect. 3.2.3. The values in brackets give the limit at which a cluster is defined as CC cluster:

- The central cooling time $t_{cool,0}$ calculated as presented in Eq. (2.24)
  (CC if $t_{cool,0} < 7.7\ Gyrs$)

- The central entropy K_0 according to Eq. (2.25)
  (CC if $K_0 < 150\ keV\ cm^2$)

- The central electron number density $n_{e,0}$ that is derived from the mass density ρ (CC if $n_{e,0} > 1.5 \cdot 10^{-2}\ cm^{-3}$)
- The central temperature drop $T_{0.00-0.04r_{500}}/T_{0.10-0.30r_{500}}$ following [Johnson et al., 2009]
  (CC if < 1)

The thresholds for the first three quantites are taken from [Hudson et al., 2009]. The boundary of the last quantity is defined in [Johnson et al., 2009].
For each halo $t_{cool,0}$, K_0 and $n_{e,0}$ are calculated as the mass-weighted median value of the ICM particles within $0.00 - 0.04\ r_{500}$. The central temperature drop results from the mass-weighted median temperature of the inner region ($0.00 - 0.04\ r_{500}$) divided by the mass-weighted median temperature of the outer region ($0.10 - 0.30\ r_{500}$). Throughout this thesis, r_{500} refers to the radius at which the density of the cluster has reached 500 times the critical density of the universe. The inner region reaches up to $0.04\ r_{500}$ to minimize the influence of direct AGN feedback on the particles [Vikhlinin et al., 2006].
In this section, a detailed analysis of the selected haloes from the *Magneticum* simulation according the four presented parameters is provided. At first, in Sect. 3.2.1, the CC and NCC fractions in *Magneticum* are derived using the four parameters to identify CC and NCC clusters. Then, Sect. 3.2.2 presents the correlation of these criteria. Finally, in Sect. 3.2.3 a new parameter for CC and NCC classification is introduced that is based on the results shown in Sect. 3.2.2.

3.2.1 CC Fractions

Table 3.1 gives an overview of all criteria with the corresponding limits and the CC and NCC fractions that are found for them in the *Magneticum* simulation. According to all four parameters, CC clusters are less common than NCC clusters with fractions of $20 - 41\%$. As a good approximation, it can be said that about one third of all clusters in the *Magneticum* simulation are CC clusters.
In the next step, the derived fractions are compared to other simulations and observations

Table 3.1: Overview of the CC fractions in the *Magneticum* simulation with four different criteria. Column (1) lists all criteria that were used and column (2) shows the corresponding notations. Column (3) presents the limits below or above which the clusters are identified as CC clusters. Column (4) and (5) give the CC and NCC fractions that were found.

Criterion	Notation	CC limit	CC Fraction	NCC fraction
Central cooling time	$t_{cool,0}$	$< 7.7\ Gyrs$	33%	67%
Central entropy	K_0	$< 150\ keV\ cm^2$	41%	59%
Central electron number density	$n_{e,0}$	$> 1.5 \cdot 10^{-2}\ cm^{-3}$	20%	80%
Central temperature drop	$\frac{T_{0.00-0.04r_{500}}}{T_{0.10-0.30r_{500}}}$	< 1	32%	68%

to evaluate how well the simulation reproduces the expected values. For this purpose, one

simulation [Barnes et al., 2017] and two observations [Hudson et al., 2009], [Andrade-Santos et al., 2017] are chosen. [Barnes et al., 2017] provided a census of CC clusters of 379 simulated clusters with similar mass range as the *Magneticum* sample. [Hudson et al., 2009] presented a detailed analysis of CC and NCC clusters from an X-ray flux-limited (*HIFLUGCS*) sample of 64 clusters and [Andrade-Santos et al., 2017] investigated 164 clusters of a *Planck ESZ* survey for its CC properties. Table 3.2 compares the fractions of these four surveys and gives some basic information on them.

At first view, the CC fractions from *Magneticum* do not seem to be in good agreement with other observations and simulations. As already mentioned in Sect. 2.2.2, [Andrade-Santos et al., 2017] demonstrated that the CC fractions in X-ray flux-limited surveys are overestimated by a factor of approximately 2.2 because of selection biases. Taking this into account with the *HIFLUGCS* observation, the CC fraction for the central cooling time and entropy lowers to 33% and for the central electron number density it becomes 26%. These bias-corrected values are in good conformity with the ones from *Magneticum*. The SZ value for $n_{e,0}$ and the values from the *Illustris TNG* simulation are all slightly higher (with exception of the entropy) than the ones from *Magneticum*. This could be explained by the smaller inner region that was chosen in both surveys. The general physical theory of CC clusters predicts higher densities and lower temperatures of matter towards the center. Following this, a smaller inner region leads to higher CC fractions with density, cooling time and entropy.

Generally, the analysis of the CC fractions reveals that CC and NCC clusters are produced in a ratio of nearly 2 : 3 in *Magneticum*. This fraction is in good accordance with the observations and simulations that were presented in this section. Starting from this, a more detailed investigation of the properties of the clusters in *Magneticum* can be performed.

Table 3.2: Overview of the CC and NCC fractions derived from the *Magneticum* simulation (row 1), the *HIFLUGCS* observation by [Hudson et al., 2009] (row 2), the *ILLUSTRIS* simulation by [Barnes et al., 2017] (row 3) and the *PLANCK ESZ* observation by [Andrade-Santos et al., 2017] (row 4). Column (1) shows the corresponding simulation or observation. Column (2) and (3) give basic information on the samples from the surveys, such as the mean redshift, the mass range of the clusters, the number of clusters and the inner region that was chosen for calculating the central values. Column (4) - (9) present different criteria according to which the CC and NCC fractions of the different surveys were derived.

Sample	**Information on Sample**		**Class.**	**Criterion**				
				$t_{cool,0}$ $7.7Gyrs$	K_0 $150keV\ cm^2$	K_0 $60keV\ cm^2$	$n_{e,0}$ $1.5 \cdot 10^{-2}\ cm^{-3}$	$n_{e,0}$ $0.5 \cdot 10^{-2}\ cm^{-3}$
MAGNETICUM	Redshift	$z = 0.066$						
Simulation	Mass Range	$144 - 5.27 \cdot 10^{13} M_\odot$	CC	33%	41%	29%	20%	36%
	Number	1199	NCC	67%	59%	71%	80%	64%
	Inner Region	$r < 0.04\ r_{500}$						
HIFLUGCS	Redshift	$\langle z \rangle = 0.053$						
Observation	Mass Range	$300 - 2.0 \cdot 10^{13} M_\odot$	CC	72%	72%	-	58%	-
[Hudson et al., 2009]	Number	64	NCC	28%	28%	-	42%	-
	Inner Region	$r < 0.048\ r_{500}$						
ILLUSTRIS	Redshift	$z = 0$						
Simulation	Mass Range	$120 - 5.0 \cdot 10^{13} M_\odot$	CC	70%	-	28%	-	54%
[Barnes et al., 2017]	Number	379	NCC	30%	-	72%	-	46%
	Inner Region	$r < 0.012\ r_{500}$						
Planck ESZ	Redshift	$0.025 < z < 0.30$						
Observation	Mass Range	-	CC	-	-	-	40%	-
[Andrade-Santos et al., 2017]	Number	164	NCC	-	-	-	60%	-
	Inner Region	r at $0.01\ r_{500}$						

3.2.2 CC Criteria Correlation

In this section the correlation of the four CC criteria, that were introduced in Sect. 3.2, are analysed. The entire simulated halo sample of 1199 haloes is used for this purpose and the sample is subdivided into high-mass, intermediate-mass and low-mass haloes as presented in Sect. 3.1.

Fig. 3.1 shows the central electron number density versus the central temperature drop (*left*) and the central cooling time versus the central entropy (*right*) of all 1199 simulated haloes. Circles refer to haloes that were classified as high-mass haloes, squares correspond to intermediate-mass haloes and diamonds are low-mass haloes. All haloes are color-coded according to their virial temperature. The segregation values are indicated by the vertical and horizontal dotted lines.

In Fig. 3.2 the same parameters and haloes are plotted as in Fig. 3.1. The plots are

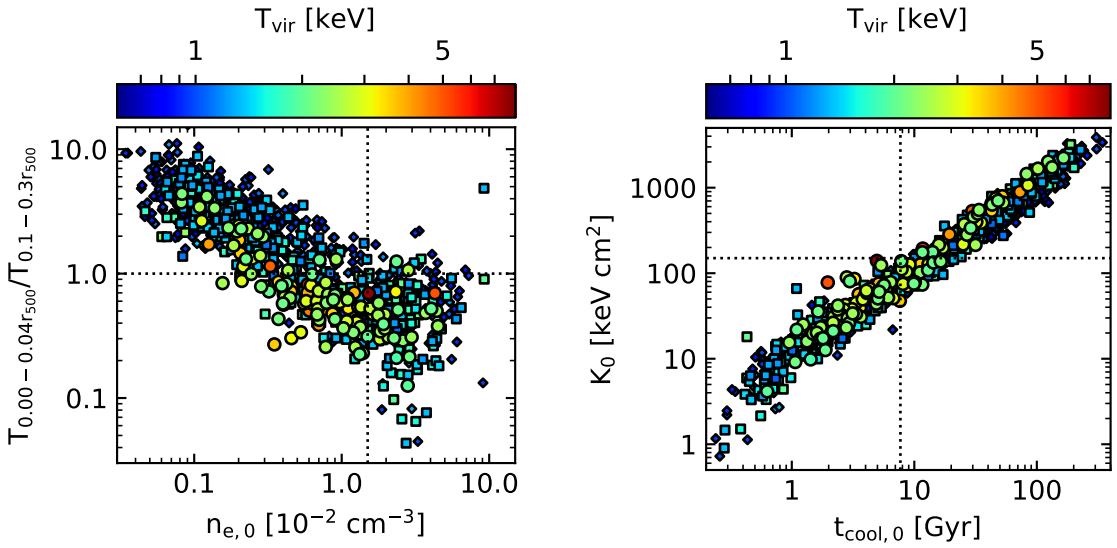

Figure 3.1: Correlation of the central electron number density versus the central temperature drop (*left*) and the central cooling time versus the central entropy (*right*) of 1199 simulated haloes. The haloes are color-coded by their virial temperature. The sample is subdivided into high-mass haloes (circles), intermediate-mass haloes (squares) and low-mass haloes (diamonds). The vertical and horizontal dotted lines represent thresholds on the quantities which segregate the sample into CC and NCC cluster. K_0, $t_{cool,0}$ and $n_{e,0}$ are the mass-weighted median values of the ICM particles within a region of $0.00 - 0.04\ r_{500}$. The central temperature drop is calculated by dividing the mass-weighted median temperature of the inner region ($0.00 - 0.04\ r_{500}$) by the mass-weighted median temperature of the outer region ($0.10 - 0.30\ r_{500}$).

additionally subdivided into three panels from top to bottom showing high-mass (circles), intermediate-mass (squares) and low-mass haloes (diamonds). The high-mass sample in-

cludes 121 haloes, the intermediate-mass sample consists of 407 haloes and the low-mass sample contains 671 haloes.

Fig. 3.2 and Fig. 3.1 demonstrate that the cluster properties are equally distributed within the selected ranges and correlate with each other. Clusters without temperature drops tend to have lower electron number densities. These clusters are referred to as NCC clusters. In contrast, haloes that show a temperature drop have higher densities and are defined as CC clusters. A similar, even stronger correlation can be found with the central cooling time and the central entropy. Low central cooling times are consistent with low entropies indicating CC clusters, whereas higher central cooling times and entropies refer to NCC clusters. The tight correlation of central cooling time and entropy is unsurprising because both parameters depend on temperature and electron number density but can be very useful as it will be stated in Sect. 3.2.3. The dotted lines segregate the cluster sample into CC and NCC clusters with fractions that correspond to the ones derived in Sect. 3.2.1. The left panels of Fig. 3.2 and Fig. 3.1 are also included in Appendix B.1. In this case, they are color-coded according to the central temperature of each halo. Therefore, it becomes apparent that a central temperature drop correlates with a high density and also with a low central temperature.

To give a direct comparison to observations, data points for the electron number density and central temperature drop for the 64 galaxy clusters from [Hudson et al., 2009] could be included into the plots. Comparing Fig. 3.1 to Fig. 5 in [Hudson et al., 2009] reveals that the correlation of the criteria from observations is in good agreement with the ones derived from the *Magneticum* simulation.

The correlation of the criteria and the conformity with observations manifest that the *Magneticum* simulation reproduces the physical properties of the central ICM very well. The correlations match the physical theory for CC clusters that predicts temperature drops, high densities, low central temperatures and therefore low central entropies and cooling times for clusters with cooling cores. A more fundamental analysis of the correlations of more parameters could be performed to further evaluate how well the predicted correlations for CC and NCC clusters are recreated but this surpasses the capacity of this thesis.

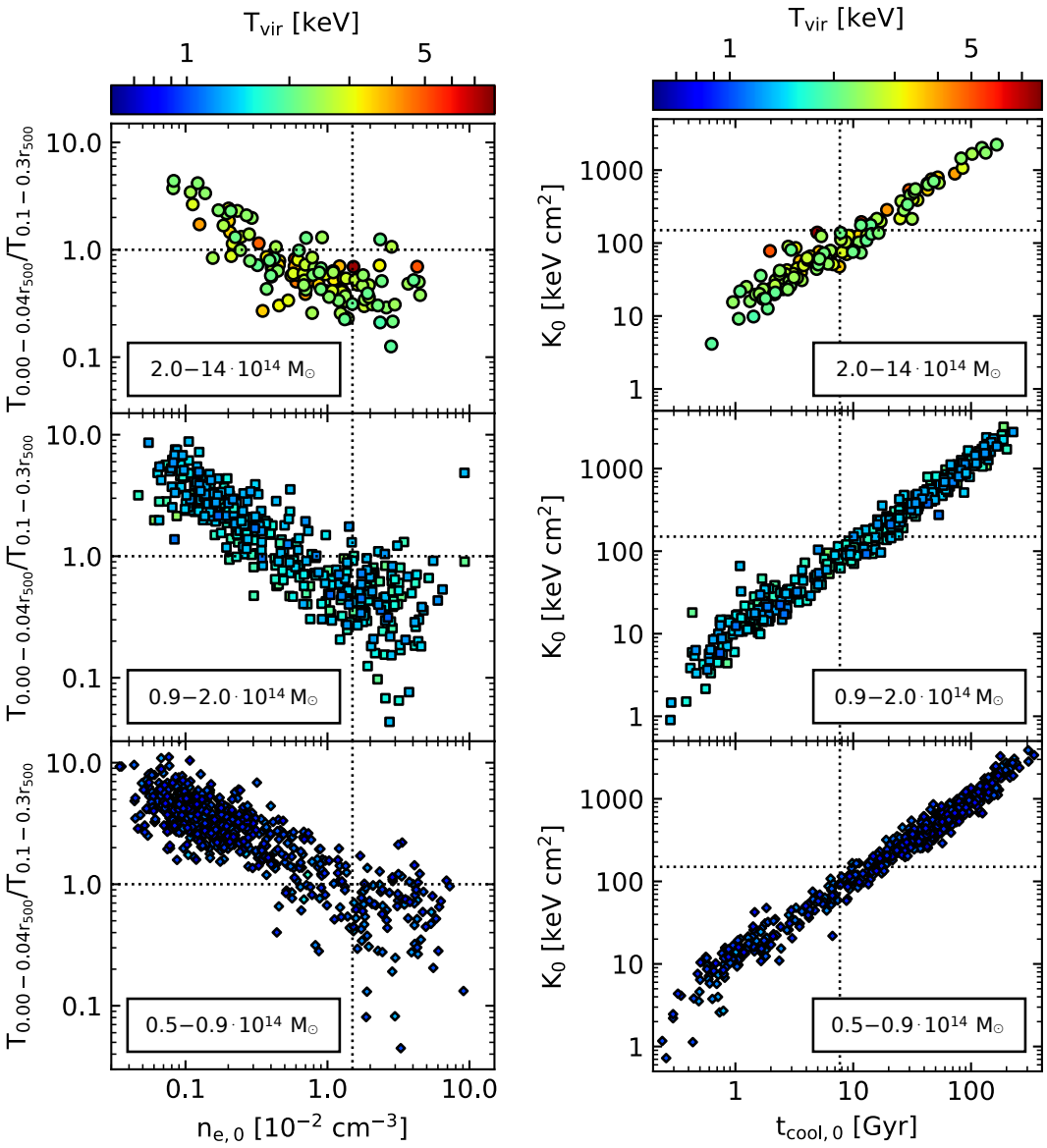

Figure 3.2: Correlation of the central electron number density versus the central temperature drop (*left*) and the central cooling time versus the central entropy (*right*) of 1199 simulated haloes. The haloes are color-coded by their virial temperature. The top panel shows the high-mass halo sample (circles), the middle one corresponds to the intermediate-mass haloes (squares) and the bottom one includes all low-mass haloes (diamonds). The vertical and horizontal dotted lines represent thresholds on the quantities which segregate the sample into CC and NCC cluster. K_0, $t_{cool,0}$ and $n_{e,0}$ are the mass-weighted median values of the ICM particles within a region of $0.00 - 0.04\ r_{500}$. The central temperature drop is calculated by dividing the mass-weighted median temperature of the inner region ($0.00 - 0.04\ r_{500}$) by the mass-weighted median temperature of the outer region ($0.10 - 0.30\ r_{500}$).

3.2.3 The Coolcoreness Parameter

In the previous section, the strong correlation of the central cooling time and central entropy was presented. [Hudson et al., 2009] found that these two criteria are the best parameters to segregate CC and NCC clusters. The results from the *Magneticum* simulation are in good accordance with the observation by [Hudson et al., 2009]. This implies that the central cooling time and entropy are also very good parameters for the *Magneticum* simulation to classify CC and NCC clusters. For this purpose, a new parameter will be introduced in this section that depends on the central cooling time and entropy of a cluster. This is the so-called "coolcoreness" of a cluster.
The coolcoreness should give a measure for how much CC a cluster is according to the central cooling time and entropy. To derive this parameter, a regression line is fitted in log-log to the right subfigure of Fig. 3.1. One of lowest haloes at the bottom left of the plot is used as starting point. This halo is assigned a coolcoreness of 100%, which means this is a definite CC cluster. Haloes that lie below this starting point are also assigned a coolcoreness of 100%. On the other hand, one of the highest haloes at the top right side is defined with 0% coolcorenesss which makes this a definite NCC cluster. Haloes that are above the defined point also have a coolcoreness of 0%. All haloes in between the start and end point are then assigned a coolcoreness according to their reference point along the regression line. The regression line fit with starting and ending point can be found in Appendix B.2.
Fig. 3.3 presents a histogram of the coolcoreness for the simulated haloes. Each bar is sub-divided into three sections. The lowest section represents the coolcoreness frequency for high-mass haloes. The middle section gives the limit for the intermediate-mass haloes and the third section refers to low-mass haloes. The height of each bar represents the frequency for the entire sample of 1199 haloes. In addition, the bars are color-coded by their value of coolcoreness. Red bars indicate NCC haloes while blue bars show CC clusters. Haloes between approximately 33% and 66% represent a transition state which is further referred to as weak CC or weak NCC clusters.

Clusters with coolcoreness between 10% and 35% are most frequent. This reflects that NCC clusters are slightly more common than CC clusters in the simulation.

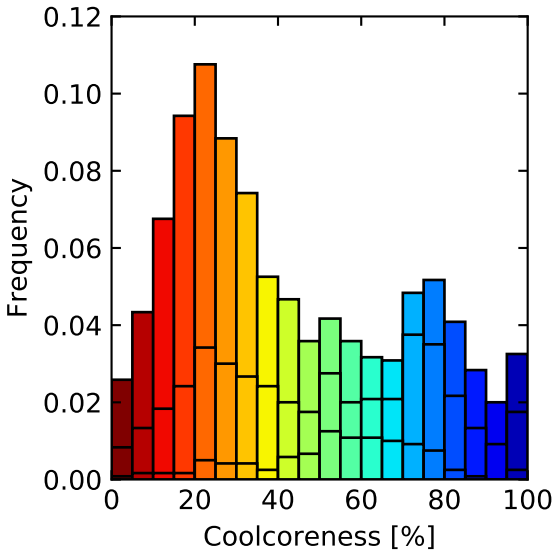

Figure 3.3: Histogram of the coolcoreness for simulated haloes. Each bar is sub-divided into three sections. The lowest section represents the coolcoreness frequency for high-mass haloes. The middle section gives the limit for the intermediate-mass haloes and the third section refers to low-mass haloes. The height of each bar represents the frequency for the entire sample of 1199 haloes. The colors refer to the coolcoreness value of the bars. Haloes with low coolcoreness are red, whereas haloes with high coolcoreness are blue.

3.3 Thermal Structure of the ICM of CC and NCC Clusters in MAGNETICUM

The fractions and correlations of CC and NCC clusters are correctly reproduced by the *Magneticum* simulation as it was stated in the previous sections. Based on these results, the following section focuses on a more detailed analysis of the structure and properties of CC and NCC clusters. Sect. 3.3.1 examines the central region of some clusters in different states. Sect. 3.3.2, on the other hand, investigates the radial profiles of some thermodynamical quantities and gas fractions to specify the thermodynamical ICM properties.

3.3.1 The Central Region

The most crucial region of the ICM to classify the state of a cluster is its central region. The behaviour of the central ICM in temperature and density determines whether a cluster is defined as CC or NCC. For this reason, three clusters in different states are selected from the high-mass sample and are examined by histograms for temperature and electron number density of their central regions. The results from Sect. 3.2.2 can be used to identify clusters that are CC or NCC according to all four parameters that were introduced. The

haloes that are chosen this way are a CC halo with halo ID 78, a weak CC halo with halo ID 0 and a NCC halo with halo ID 86.
Fig. 3.4 presents six histograms of temperature and density for the inner region particles of the three above mentioned haloes. The left panel refers to temperature histograms. The right panel is assigned to electron number density histograms. From top to bottom, the CC halo 78 in blue, the weak CC halo 0 in green and the NCC halo 86 in red are depicted. The CC halo histogram is calculated from 164 particles within the inner region, the weak CC halo encompasses 2456 particles because it is the largest halo of the sample and the NCC halo only includes 46 particles which is a direct result of its low density. The inner region from which the particles for the histogram are taken is $0.00 - 0.04\ r_{500}$.
The CC halo shows a high peak at low temperatures and a trend to higher densities. On the contrary, the NCC cluster lacks a peak at low temperatures and has more particles with higher temperature than the CC cluster. The weak CC cluster shows more particles than the NCC but less particles than the CC at lower temperatures. Its temperature stretches to higher temperatures than the ones of the CC cluster but it does not reach as high temperatures as the NCC cluster. The electron number density of the CC cluster depicts a relatively broad distribution with a trend to higher densities. In contrast, the NCC cluster includes only particles with very low densities. The weak CC cluster in this case has even higher densities than the CC cluster in complete absence of low densities.
The basic theory of CC and NCC clusters assumes that CC clusters reveal matter with low temperature and high densities in their central regions. Conversely, NCC clusters are supposed to show higher temperatures and lower densities. Following this, a weak CC cluster would be a compromise of these two cases. The histograms of Fig. 3.4 depict these postulated properties very well. The only exception is that the weak CC cluster has higher densities than the CC cluster. A possible explanation for this, could be that the particles in the histogram would need to be weighted by mass. Heavier particles contribute stronger to temperature and density and could therefore explain the discrepancy in the density of the CC and weak CC cluster.
In general, it can be deduced that the ICM particles in the central region of clusters follow the behaviour that is predicted in theory. Mass-weighted histograms with higher resolution could be created to conduct a more improved analysis.

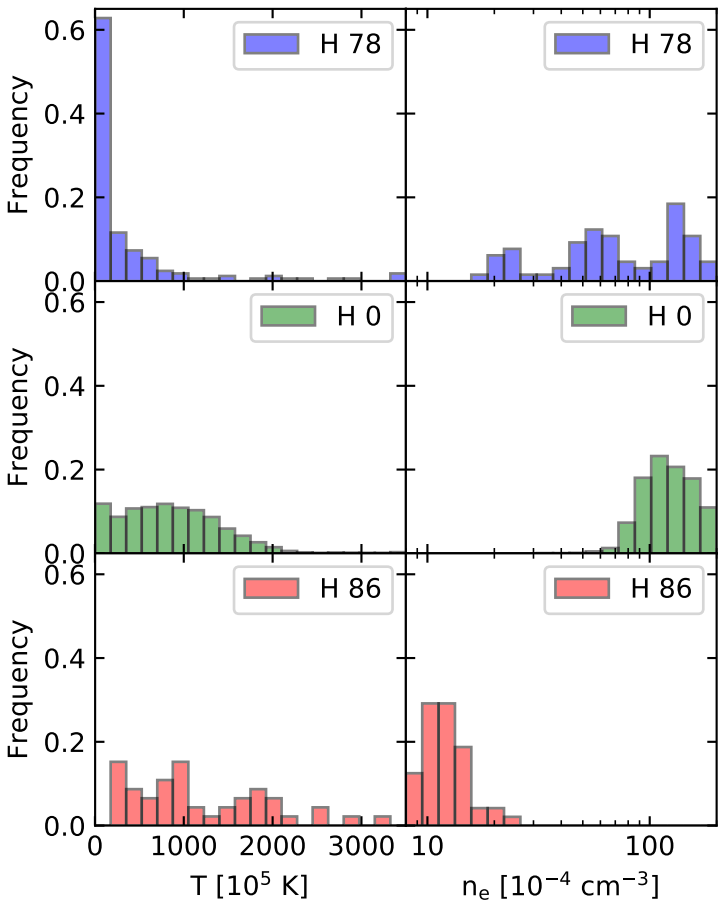

Figure 3.4: Histograms of temperature and electron number density for the ICM particles within the inner regions ($0.00 - 0.04\ r_{500}$) of three simulated haloes. The three haloes are selected from the high-mass sample. The top panel with blue bars corresponds to the CC Halo 78 that contains 164 particles within its inner region. Halo 0 in the middle panel with green histograms is a weak CC cluster. It encompasses 2456 central particles. The bottom panel Halo 86 is defined as NCC halo with 46 particles and depicted in red color.

3.3.2 Radial Profiles of CC and NCC Clusters

In this section the radial profiles of thermodynamical quantities for CC and NCC clusters are compared. Subsequently, cumulative and differential gas fraction profiles are presented. The main goal of this examination is to further understand the thermodynamical structure and properties of the ICM that come along with CC and NCC clusters.
For the investigations done in this section, several haloes from the simulation have to be selected. To compare the main properties of CC and NCC cluster profiles, some CC and NCC clusters from the different mass ranges are identified. The clusters are classified as

CC or NCC clusters according to all four criteria that were used in the previous sections. Table 3.3 lists all chosen clusters and their masses.

Table 3.3: Overview of the clusters that were selected as CC and NCC clusters according to all criteria. Column (1) refers to the mass sample, column (2), (3), (4) and (5) list the IDs and M_{500} masses of the chosen CC and NCC haloes for each mass sample

Sample	**CC Clusters**		**NCC Clusters**	
	Halo ID	M_{500} [10^{14} $M_\odot$]	Halo ID	M_{500} [10^{14} $M_\odot$]
High-mass Clusters	71	2.10	95	2.19
	138	2.20	107	2.29
	195	2.17	86	2.88
Intermediate-mass Clusters	494	1.09	575	1.00
	346	1.35	261	1.35
	467	1.26	140	1.96
Low-mass Clusters	567	0.85	613	0.61
	1213	0.71	1550	0.56
	943	0.57	1013	0.64

Temperature Profiles

In Fig. 3.5 the temperatures of three CC and three NCC clusters for each mass range are plotted against their radii. Temperatures T/T_{500} and radii r/r_{500} are scaled to the values where the density of the cluster has reached 500 times the critical density of the universe. The left column contains high-mass haloes, the middle one refers to intermediate-mass haloes and the right one presents results for low-mass haloes. The top panel with continuous blue lines shows three CC haloes for each mass range. Likewise, the bottom panel contains three NCC haloes for each mass range. The errors are given with 1-σ deviation and are indicated by the shaded regions.. The profiles are derived from radial bins of the temperature of the ICM particles. For each bin the mean mass-weighted temperature of all particles within the bin is determined. The bins start at a bin-size of 100 (high-mass sample), 70 (intermediate-mass sample) and 50 (low-mass sample) particles and then the particle number increases linearly with the number of bins that were executed.

Starting from $r/r_{500} = 1.0$, all cluster profiles (CC and NCC haloes) show a similar behaviour down to $r/r_{500} \approx 0.2$. The scaled temperatures rise from $T/T_{500} = 1$ up to $T/T_{500} \approx 1.6 - 1.7$. Then, the profiles begin to differ widely for CC and NCC clusters. From $r/r_{500} \approx 0.2$ to $r/r_{500} \approx 0.045$, the temperatures of CC clusters drop to $T/T_{500} \approx 0.5$. In contrast, the NCC profiles continue to rise but with smaller slopes than before and small drops in between. Below $T/T_{500} \approx 0.5$, all profiles increase steeply. This region is excluded for the following investigations because it is probably not resolved high enough or suffers from too strong AGN feedback.

[Baldi et al., 2012] reported a detailed analysis of temperature profiles from a sample of 12 *XMM Newton* clusters. The basic results of this study are summarized in the following. All clusters show a decline in temperature from 0.15 r_{500} to 1.0 r_{500}. CC clusters are found to have central temperature drops, whereas NCC clusters reveal increasing or flat profiles towards the center. CC and NCC profiles only differ in the inner regions ($r < 0.15$ r_{500}),

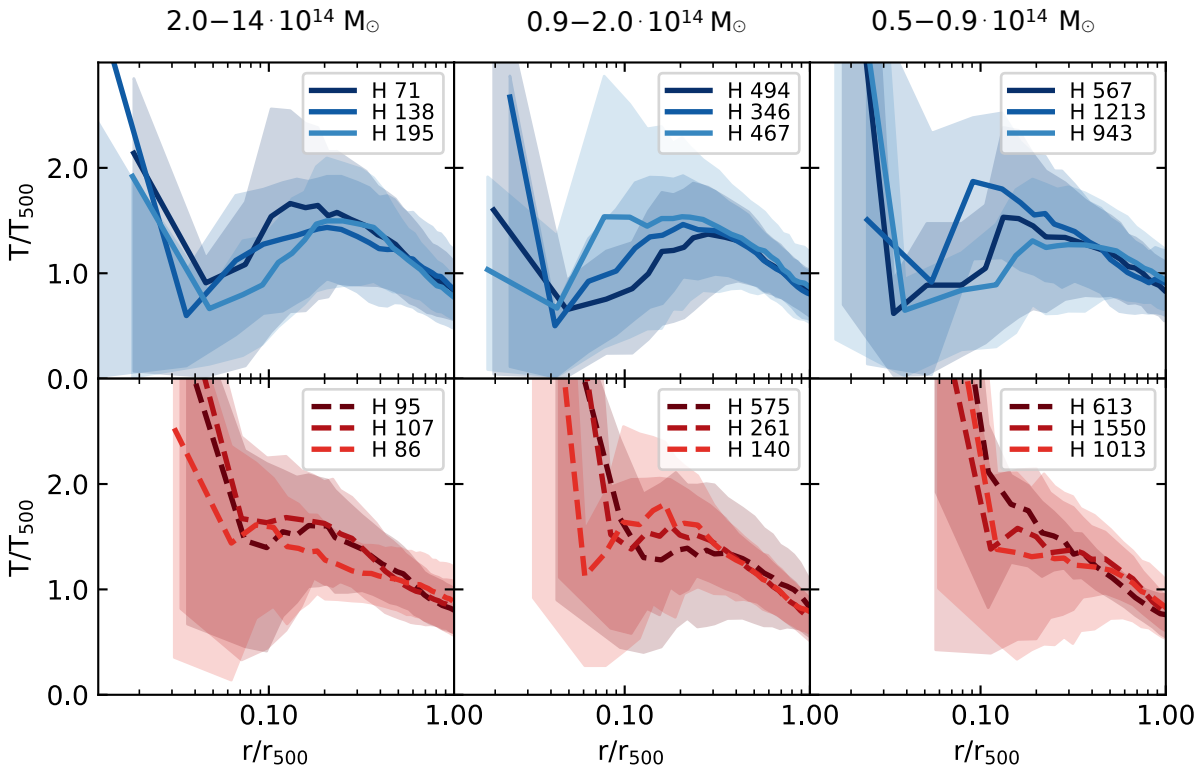

Figure 3.5: Scaled temperatures of three CC and three NCC clusters for each mass range plotted against their scaled radii. Temperatures T/T_{500} and radii r/r_{500} are scaled to their values where the density of the cluster has reached 500 times the critical density of the universe. The left column contains high-mass haloes, the middle one refers to intermediate-mass haloes and the right one presents results for low-mass haloes. The top panel with continuous blue lines shows three CC haloes for each mass range. Likewise, the bottom panel contains three NCC haloes for each mass range. The errors are given with 1-σ deviation and are indicated by the shaded regions.

the outer regions seem to be quite similar. Comparing this to the temperature profiles in Fig. 3.5, a very similar behaviour can be identified. Thus, the simulated and observed profiles are in quite good agreement.

Electron Number Density, Cooling Time and Entropy Profiles

In Fig. 3.6 the electron number density, cooling time and entropy of CC and NCC clusters is plotted against the scaled radius r/r_{500}. From left to right the high to low-mass haloes are depicted. The top panel shows radial electron number density profiles, the middle one refers to radial cooling time profiles and the bottom one presents radial entropy profiles of the ICM. The continuous blue lines represent CC clusters, while the dashed red lines show NCC clusters. All errors are given with a 1-σ deviation and are indicated by the shaded regions. The profiles are derived from radial bins of the temperature of the ICM

particles. For each bin the mean mass-weighted temperature of all particles within the bin is determined. The bins start at a bin-size of 100 (high-mass sample), 70 (intermediate-mass sample) and 50 (low-mass sample) particles and then the particle number increases linearly with the number of bins that were executed.

For these profiles the same characteristics as with the temperature profiles can be identified. The outer regions (0.2 r_{500} - 1.0 r_{500}) are quite similar for each quantity, while the inner regions differ for CC and NCC clusters. The electron number densities of CC clusters show steep increases towards the center and differ from the NCC clusters in nearly two magnitudes. Cooling time and entropy profiles of CC clusters steeply decline towards the center also differing from NCC clusters in nearly two magnitudes.

The profiles can be compared to different observations. [Pratt et al., 2009] published an examination of the entropy profiles of 31 *XMM-Newton* clusters that can be compared to the high-mass sample of Fig. 3.6. [Sanderson et al., 2006] presented cooling time profiles of 20 Chandra clusters scaled to their r_{500} radius. The up-following survey of the same clusters in [Sanderson et al., 2009b] derived the gas density versus scaled radius that would be useful for a comparison with the electron number density. At first sight, these profiles seem to fit to the ones simulated. For a more precise comparison the data from the observations should be added in Fig. 3.6.

In summary, it can be said that for the simulated CC and NCC clusters, a great difference in the inner regions of all investigated radial profiles is visible. The simulated cluster outskirts ($r/r_{500} \approx 0.2$ to $r/r_{500} = 1.0$) of all radial profiles are very similar to each other and thus behave in a self-similar scaling fashion. [Kravtsov and Borgani, 2012] summarized the nature of all scaled radial profiles of thermodynamical quantities the following way:

1. For radii $r < r_{2500}$ the largest scatter in profiles can be observed; here the profiles differ widely from a self-similar scaling

2. For radii between $r_{2500} < r < r_{500}$ the smallest scatter is found and the scaling of clusters is quite self-similar

3. For radii larger than $r > r_{500}$ scatter is expected to increase again with radius but these regions have not been observed in a sufficient way.

The relationship between r_{2500} and r_{500} is $r_{2500} \approx 0.4\ r_{500}$. Thus, point one and two can be confirmed quite well with the presented profiles. The results shown above, imply that the hydrodynamical effects that cause the distribution of CC and NCC clusters are nearly restricted to the central regions of clusters. At the outskirts, gravitational forces are supposed to dominate and the thermodynamical structures that are used to identify CC or NCC clusters vanish.

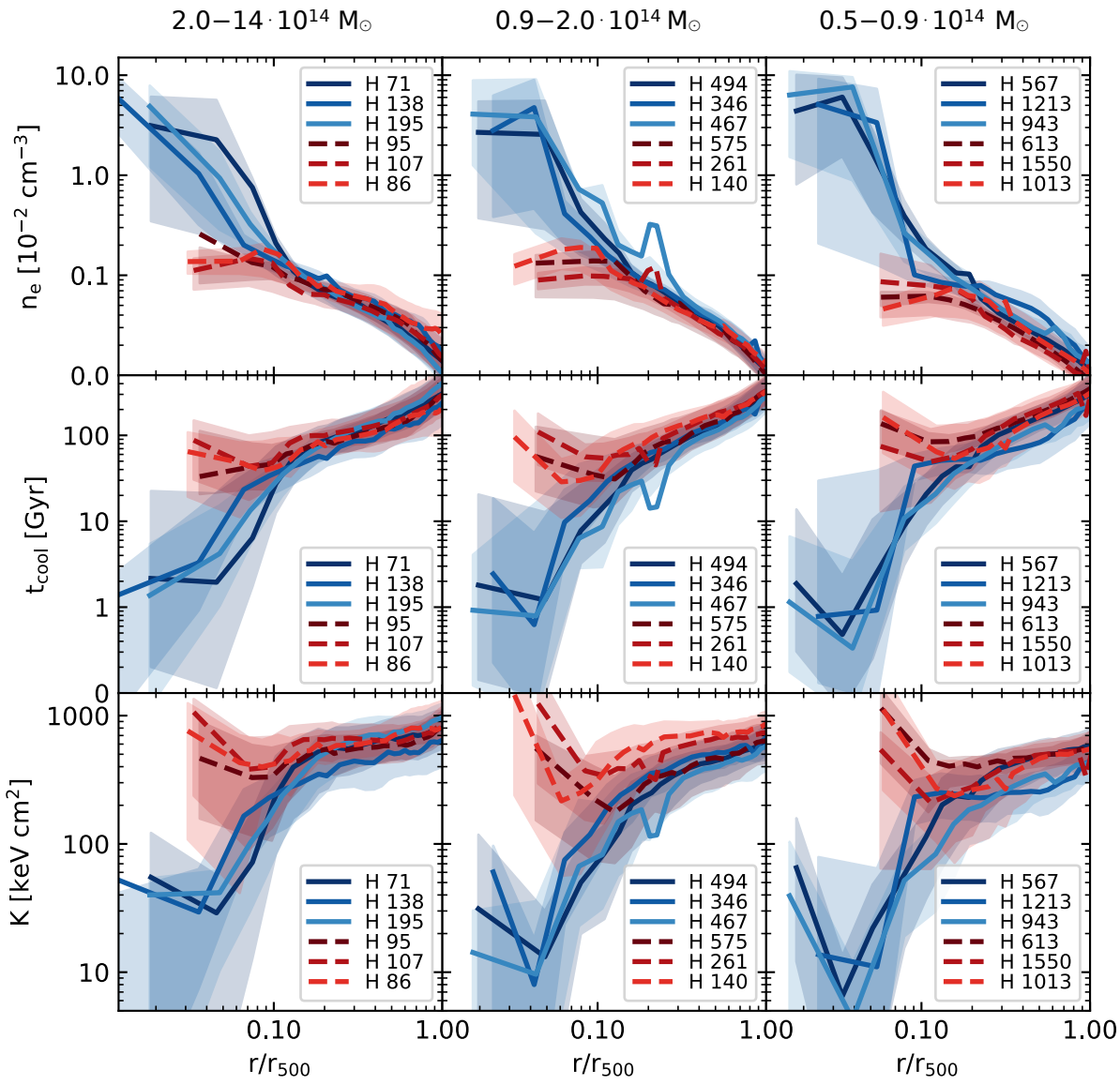

Figure 3.6: Electron number density (*top*), cooling time (*middle* and entropy (*bottom*) of three CC and three NCC clusters for each mass range plotted against their scaled radii. The radii r/r_{500} are scaled to their values where the density of the cluster has reached 500 times the critical density of the universe. From left to right the high-mass to low-mass haloes are depicted. The continuous blue lines represent CC clusters, while the dashed red lines show NCC clusters. All errors are given with a 1-σ deviation and are indicated by the shaded regions.

Gas Fraction Profiles

Gas fraction profile plots are a useful measure to evaluate how well the ICM properties of clusters are reproduced. In this section, the median cumulative and differential gas fraction

profiles of the simulated clusters are presented and compared to another simulation and observations.
For the cumulative profile, only the high-mass sample of the *Magneticum* sample is chosen to ensure a better comparison with the observation. Likewise, for the differential profile a sub-sample of haloes from the high-mass sample is selected to ensure a halo sample with similar masses as the observation. For each halo, the cumulative and differential gas fractions are calculated in radial bins. This means that in each radial bin the masses of all particles and the masses of the gas particles are summed up separately. Then, the gas mass is divided by the total mass which returns the gas fraction value of this bin. Finally, the median cumulative and differential gas fraction profiles are derived from the bins of all haloes. The result is shown in Fig. 3.7 as a blue continuous line.
To compare the gas fractions with another simulation, the median gas fractions that were derived from the *IllustrisTNG* simulation [Barnes et al., 2017]) are included. These curves are indicated by the dashed-dotted green lines in Fig. 3.7. The dashed red lines refer to observations. For the cumulative gas fraction on the left, the median gas fraction of 31 *XMM-Newton* clusters is used ([Pratt et al., 2009]). The differential gas fraction on the right shows results from a survey of 35 *Chandra* clusters by [Landry et al., 2012]. The dotted black lines in both plots are the universal baryon fraction Ω_B/Ω_M by [Komatsu et al., 2011].
The samples have different median mass values that are presented in the following. The *Magneticum* high-mass sample for the cumulative profile gives a median mass of $M_{median} = 2.78 \cdot 10^{14}\ M_\odot$. The sub-sample for the differential gas fraction profile plot is higher with $M_{median} = 5.35 \cdot 10^{14}\ M_\odot$. *IllustrisTNG* presented a median mass value of $M_{median} = 2.78 \cdot 10^{14}\ M_\odot$. The observation by [Pratt et al., 2009] reveals a median mass of $M_{median} = 2.59 \cdot 10^{14}\ M_\odot$ and the one by [Landry et al., 2012] hosts a median mass of $M_{median} = 5.40 \cdot 10^{14}\ M_\odot$. Thus, the *Magneticum* gas fraction profiles can be compared quite well with the observations.
In the cumulative gas fraction profile, the inner region ($0.01\ r_{500} - 0.06\ r_{500}$) of all three profiles behave nearly equal but from $0.06\ r_{500}$ to $1.00\ r_{500}$ the gas fractions start to differ greatly. *IllustrisTNG* rises much steeper than the other profiles and finally flattens at $0.5\ r_{500}$ [Barnes et al., 2017]. *Magneticum*, on the contrary, rises more slowly than the [Pratt et al., 2009] profile but shows a more similar increase than *Illustris*. In the differential plot, *Magneticum* fits perfectly to the observations between $0.5\ r_{500}$ and $0.8\ r_{500}$ but drops too steep towards the center. [Barnes et al., 2017] is in similar with *Magneticum* at the central region but departs drastically towards the outer regions.
In summary, the *Magneticum* simulation reproduces the observed profiles properly especially at the outer regions. The simulated profiles fit better to the observations than the *IllustrisTNG* simulation. The only problem with *Magneticum* profiles is that they do not rise steeply enough. [Barnes et al., 2017] assumed that their profiles rose too steeply because of too strong AGN feedback. Applying this to *Magneticum*, the AGN feedback in this simulation could be too weak.

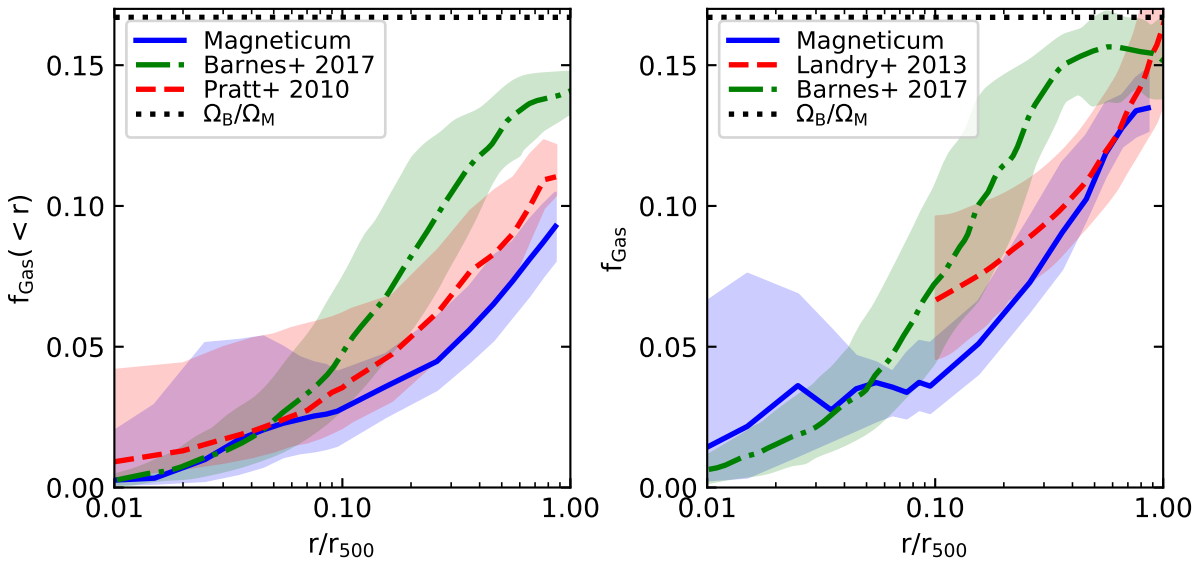

Figure 3.7: Median cumulative and differential gas fractions. (*left*) Median cumulative gas fraction of the *Magneticum* high-mass sample (blue continous line), the *IllustrisTNG* high-mass sample [Barnes et al., 2017] (green dash-dotted line and the observed median profile by [Pratt et al., 2009] (red dashed line). (*right*) Median differential gas fraction of a sub-sample of the *Magneticum* high-mass sample (blue continous line), the *IllustrisTNG* high-mass sample [Barnes et al., 2017] (green dash-dotted line and the observed median profile by [Landry et al., 2012] (red dashed line). All errors are given at 1-σ deviation. The dotted black line is the universal baryon fraction Ω_B/Ω_M by [Komatsu et al., 2011].

3.4 Coolcoreness, Relaxation and Scatter in Scaling Relation in MAGNETICUM

The previous section stated that the *Magneticum* simulation produces CC and NCC clusters in relatively good accordance with observations. Thus, the simulation data can be used to investigate a theory that is quite contradictory to CC clusters. In Sect. 2.2.3 several models were introduced that try to explain the CC - NCC distribution of clusters. One cyclic model predicts that CC clusters are the "natural" state of clusters and that NCC clusters only develop after major mergers [Hahn et al., 2015]. According to this theory, NCC clusters are supposed to be disturbed structures and in contrast, CC cluster should show relaxed morphologies. In addition, the question as to whether CC clusters are connected to relaxed morphologies is closely linked to the question of the origin of scatter along scaling relations. Both topics are investigated briefly in this section. The first subsection opposes the above introduced coolcoreness parameter to two parameters that are often used to identify disturbed clusters. Subsequently, in the second subsection, the scatter of CC and NCC clusters along the T-M scaling relation is examined.

3.4.1 Coolcoreness and Relaxation Parameters

Two parameters that are commonly used to evaluate whether a cluster was recently disturbed by a merger, are the center shift w and the mass ratio $M_{sat}/M_{satellite}$. Observations such as the ones performed by [Sanderson et al., 2009a], have confirmed that the center shift w is a good indicator for a dynamical active state. This center shift is defined as the projected offset between the X-ray centroid in the surface brightness of a cluster and the position where the brightest central galaxy of the cluster (BCG) can be found [Sanderson et al., 2009a]. The mass ratio is used as a similar indicator. It can be derived by dividing the stellar mass of the largest satellite galaxy by the mass of the central dominant (cD) galaxy of a cluster.
Fig. 3.8 shows the center shift (left panel) and the mass ratio (right panel) versus the coolcoreness of each halo color-coded by their virial masses. The center shift is given in units of r_{500}.

In both plots no correlation between the two parameters and the coolcoreness of the

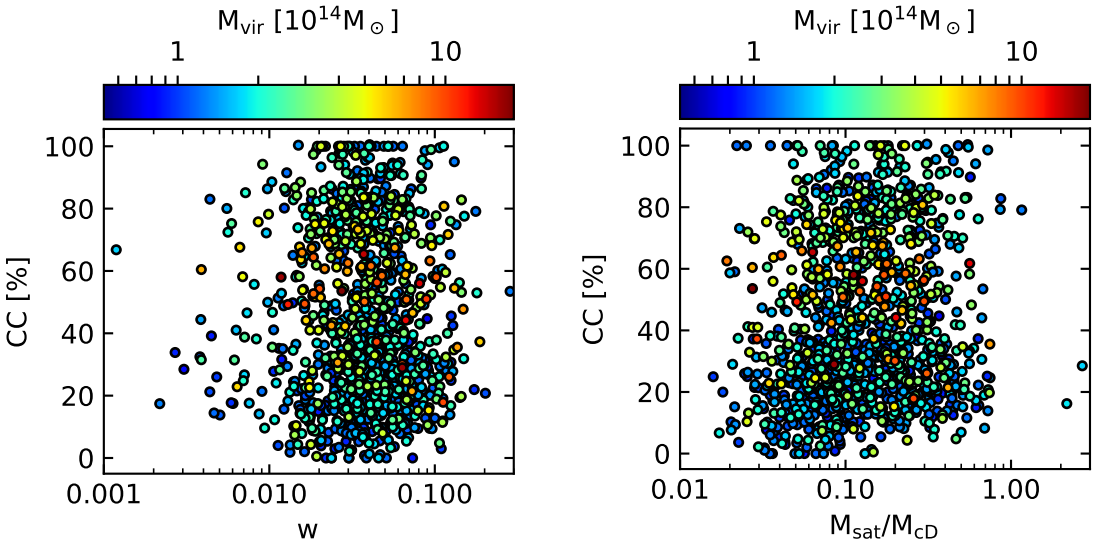

Figure 3.8: Center shift (*left*) and mass ratio (*right*) versus the coolcoreness of each halo color-coded by its virial mass. The center shift is defined as the deprojected offset of the peak in the X-ray surface brightness profile and the position of the BCG. The mass ratio is defined as the mass of the largest satellite galaxy divided by the mass of the central dominant galaxy. The coolcoreness of each halo is defined as presented in Sect. 3.2.3.

clusters can be found. CC as well as NCC clusters have high and low center shifts and mass ratios. The haloes are equally distributed according to their mass and both criteria. The left panel of Fig. 3.8 can be compared to a observation by [Boehringer et al., 2010]. This survey includes a sample of 31 clusters by *ROSAT* that was reobserved with *XMM-*

Newton. [Boehringer et al., 2010] presented plot of the center shift w as a function of the M_{500} mass. The clusters of this plot are subdivided into CC and NCC clusters. Similar to *Magneticum* the center shift does not depend on the cluster masses [Boehringer et al., 2010]. Also, several CC haloes with higher center shift were found but generally the paper presented that CC cluster are the most regular ones.
In summary, it can be concluded that the state of clusters in the *Magneticum* simulation does not correlate with the two investigated morphology parameters. The distribution of the values of the parameters with cluster masses fits relatively adequate to observations. The considered observation of the center shift does not show a strong correlation of center shift with cluster state but reveals a trend of CC clusters to be the more relaxed ones. Further investigations of more morphology parameters would be needed to confirm or disprove a correlation of coolcoreness and relaxation. In this context, it would also be necessary to evaluate how well the chosen parameters actually indicate a disturbed morphology [Boehringer et al., 2010].

3.4.2 Coolcoreness and the T-M Scaling Relation

The correct reproduction of scaling relations is a key feature of cosmological simulations. [Biffi et al., 2012] presented that the $L_X - T$ scaling relation of *Magneticum* clusters is in good conformity with observations. In the following, the $T - M$ scaling relation will be used for further investigations. In Append. A.4 a short derivation of this scaling relation is provided. To summarize, scaling relations give the dependence of physical properties on mass. Therefore, in a first approach, it is assumed that structures such as clusters only form due to the gravitational force. Using this assumption, the T-M scaling relation can be derived, which shows a simple power-ratio dependence of the temperature on mass according to the following equation:

$$T \propto (E(z)M_\Delta)^{2/3}\,, \tag{3.1}$$

with M_Δ being the mass that is enclosed up to a radius where the density of the cluster has reached a specific overdensity with respect to a reference density. T refers to the temperature measured at this overdensity. $E(z)$ is defined in the cosmological model as a function of redshift z: $E^2(z) = \Omega_m(1+z)^3 + \Omega_\Lambda$. [Boehringer et al., 2011], [Nagai and Dolag, prep] This scaling relation has been confirmed by many observations (e. g. [Vikhlinin et al., 2005]). Up-following more detailed analyses of scaling relations try to explain the origin of the observed scatter among scaling relations. Some authors propose that this scatter is dominated by merger events and thus can be assigned to disrupted morphologies [Smith et al., 2005]. However, other simulations and observations revealed that the scatter originated from phenomena such as an early pre-heating by AGNs [Balogh et al., 2006] or even radiative cooling in CC clusters [O'Hara et al., 2006] and cannot be assigned to mergers. As stated above, the clusters from the simulation show no evidence for a correlation of their morphologies and their states. Therefore, it is interesting what kind of correlation

between the coolcoreness and scatter in the scaling relation can be found.
Fig. 3.9 shows the virial temperature mass relation of all simulated clusters color-coded by their coolcoreness. The best regression line fit is inserted as a black line. The fit was executed on the logarithmic mass temperature data according to $\log(T_{vir}) = m \cdot \log(M_{vir} + t)$. This results in a temperature mass dependency of $T = \beta \cdot 10^{\alpha}$ with $\beta = 10^{t}$ and $\alpha = m$. For the entire sample the best fitting values are $\alpha = 0.63$ and $\beta = 0.88$.
α can be compared to the value of 2/3 from Eq. (3.1) which is in very good agreement. In addition, this value can also be compared to observational results. For example, [Vikhlinin et al., 2005] determined a mass-temperature relation of $M_{500} \propto T^{\gamma}$ with $\gamma = 1/\alpha = (1.5 - 1.6) \pm 0.1$ of 13 low-redshift relaxed cluster from *Chandra*. The value from *Magneticum* lies within this range and is therefore well confirmed.
Fig. 3.10 presents a detailed analysis of the scatter of the clusters among the scaling re-

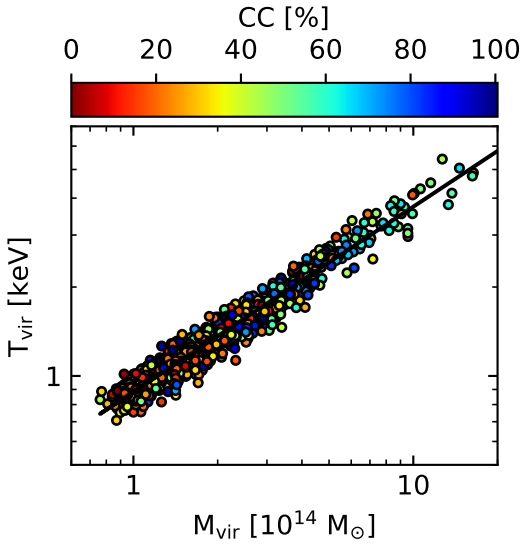

Figure 3.9: Scatterplot of virial temperature versus virial mass of each cluster color-coded by their coolcoreness. The regression line fit is indicated by the black line.

lation. The halo sample is subdivided into three groups shown from the top to the bottom panels. The top panels in blue color show CC clusters with coolcoreness above 66%, the middle ones in green contain all clusters with coolcoreness between 33% and 66% and the bottom panels in red present NCC clusters with coolcoreness below 33%. The plots on the left display the T-M scaling relations for each coolcoreness range with regression lines. In the middle, the relative errors of the haloes with respect to the regression line are shown in scatterplots and the right column depicts histograms of these relative errors. Different deviation values of the histograms and fitting values the scaling relations are presented in Table 3.4.

Fig. 3.10 as well as Table 3.4 reveal that no great difference among the scatter in the

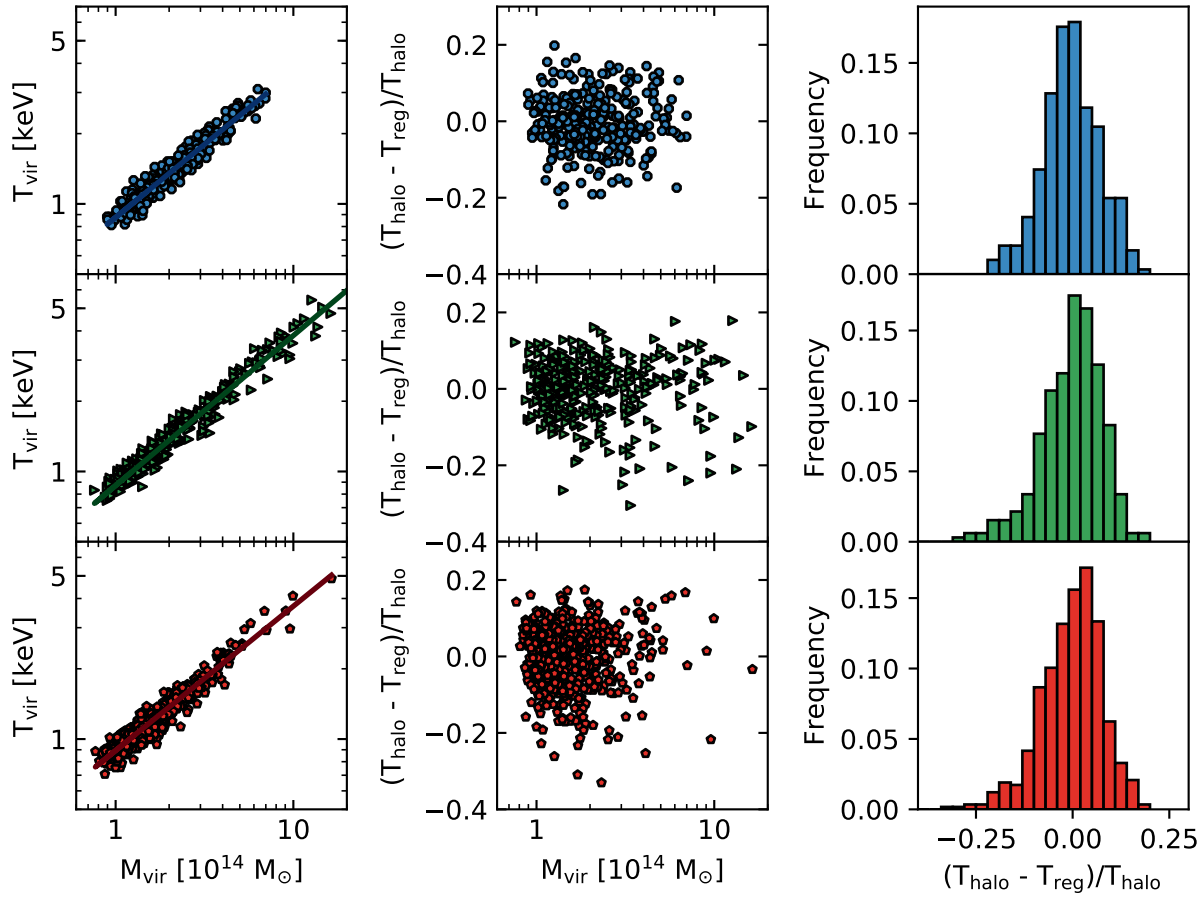

Figure 3.10: This figure gives a detailed analysis of the scatter of the haloes along the T-M scaling relation. The haloes are subdivided into three sample from top to bottom (blue, green, red): clusters with coolcoreness above 66%, between 33% and 66% and below 33%. From left to right the following plots are shown: (1) Virial mass versus virial temperature of each coolcoreness sample with fitted regression line, (2) relative errors of the haloes to the regression line agains the virial mass, (3) histograms of the relative errors of the haloes to the regression lines.

T-M scaling relation is detectable. A slight trend for CC clusters to have the lowest scatter is recognized. Surprisingly, the weak CC and weak NCC clusters show the highest scatter. If it was assumed that the scatter among the T-M scaling relations depends on the morphology of a cluster [Smith et al., 2005], then the lowest scatter for CC clusters and highest scatter for NCC clusters would be expected. This correlation cannot be stated cleary from the results of the simulated clusters. The trend of CC clusters to be more relaxed than NCC or weak CC clusters could be confirmed. However, the reason for the higher scatter of weak NCC clusters than of NCC clusters would need to be clarified. If the scatter, on the contrary, was dominated by an early preheating effect such as AGN

Table 3.4: Fitting parameters of the T-M scaling relation and histogram parameters of the relative error from the scatter of the T-M scaling relation. The table is subdivided into three groups that were investigated for these parameters. Haloes with coolcoreness above 66%, between 33% and 66% and below 33%. Column (2) contains the number of haloes of each sample. Column (3) - (7) are the mean value, standard deviation and 1 to 3 σ percentiles distances of the relative errors of the haloes to the regression line of each sample. Column (8) and (9) are the fitting parameter values of the regression lines.

Sample	Number	Histogram Parameters					Fitting Parameters	
		Mean	σ	1-σ Dist.	$2-\sigma$ Dist.	$3-\sigma$ Dist.	α	β
CC > 66%	296	-0.0027	0.073	0.143	0.298	0.393	0.625	0.87
66% > CC > 33%	326	-0.0030	0.079	0.144	0.332	0.466	0.642	0.87
CC > 66%	296	-0.0030	0.079	0.151	0.325	0.487	0.618	0.89

feedback [Balogh et al., 2006], then the investigation of this scatter could not be used to identify an existing or non-existing correlation of cluster state and morphology. In this case, the results presented above, would imply that physical processes that dominate in weak CC or weak NCC clusters, are the reason for scatter among the scaling relation.
In general, it has to be said, that a more detailed analysis for the reason of scatter among the scaling relation especially from observations would be necessary. In this study only the virial temperature-mass scaling relation was investigated. The radial profiles of Sect. 3.3.2 revealed that CC and NCC clusters show quite similar - nearly self-similar - profiles at their outskirts. Thus, to elaborate whether the scatter in scaling relations depends on the state and therefore on the thermodynamical properties of a cluster, it would be necessary to compare the scatter along a temperature-mass relation at r_{2500}.

4 Conclusions

In this study, the ICM properties of 1199 NCC and CC clusters simulated with the *Magneticum Pathfinder* simulation were investigated. The cluster sample was selected from simulation *Box2/hr* which expands over a range of 352 Mpc/h and comprises $2 \cdot 1583^3$ particles in high resolution. The mass range of the clusters spans from $1.44 \cdot 10^{15}\ M_\odot - 5.27 \cdot 10^{13}\ M_\odot$. Snapshot 136 from the simulation run was chosen which corresponds to a low redshift of $z = 0.066$.
The CC fractions of the cluster sample and correlation of parameters were examined using four different criteria. Furthermore, the thermal structure of the ICM of several clusters was examined using histograms and radial profiles. At last, the correlation of the state of a cluster, its relaxation morphology and the scatter in scaling relations was probed.
The main results of these studies are summarized in the following:

1. The ratio of CC and NCC clusters of the simulated cluster sample is nearly 2 : 3 using four different parameters. The fractions are in good agreement with bias corrected fractions of X-ray flux-limited samples [Hudson et al., 2009] and SZ samples [Andrade-Santos et al., 2017].

2. The correlation of the four criteria manifests that clusters with high central electron number density show temperature drops and low central temperatures.

3. The correlation of central cooling time and central entropy was used to introduce a new parameter. The coolcoreness parameter determines how much CC each cluster is.

4. The radial profiles of the simulated CC and NCC clusters show different behaviour at inner radii but behave similar at outer radii. Between $0.045 - 0.2\ r/r_{500}$ there is a huge difference in the thermodynamical properties of CC and NCC clusters. From $0.2 - 1.0\ r/r_{500}$ this difference vanishes and the clusters scale strongly self-similar.

5. The simulated cumulative and differential gas fraction profiles are only slightly lower than the observed ones but apart from that fit quite well. Following [Barnes et al., 2017] it could be assumed that the AGN feedback of the simulation is too weak.

6. The state of the simulated clusters as CC or NCC does not correlate with the two investigated morphology parameters. For the center shift this is in good conformity with the observation by [Boehringer et al., 2010] who also found no correlation between center shift and CC or NCC state of a cluster. This means, that following the simulation, CC clusters are not more relaxed than NCC clusters.

7. The virial temperature mass scaling relation is reproduced quite well. The fitted slope agrees with the slope derived from observations (e.g. [Vikhlinin et al., 2005]). The scatter along the T-M scaling relation of the simulated clusters depends only weakly on the state of a cluster. CC clusters show the lowest scatter, whereas weak CC and weak NCC clusters reveal the highest scatter.

Concluding, it can be summarized that the *Magneticum Pathfinder* simulation reproduces the CC and NCC fractions of clusters very well. The profile plots show that the thermodynamical properties of the ICM are captured correctly and that the underlying physical models fit. A further investigation of the processes leading to the lower gas fractions within the clusters should be undertaken. Upcoming studies could concentrate on an examination of how the CC and NCC distribution develops. The results presented in this thesis indicate that merger events cannot or cannot solely be the reason for the different core states of clusters.

Bibliography

[Andrade-Santos et al., 2017] Andrade-Santos, F., Jones, C., Forman, W. R., Lovisari, L., Vikhlinin, A., van Weeren, R. J., Murray, S. S., Arnaud, M., Pratt, G. W., Démoclès, J., Kraft, R., Mazzotta, P., Boehringer, H., Chon, G., Giacintucci, S., Clarke, T. E., Borgani, S., David, L., Douspis, M., Pointecouteau, E., Dahle, H., Brown, S., Aghanim, N., and Rasia, E. (2017). The fraction of cool-core clusters in x-ray versus SZ samples using chandra observations. *The Astrophysical Journal*, 843(1):76.

[Baldi et al., 2012] Baldi, A., Ettori, S., Molendi, S., and Gastadello, F. (2012). Self-similarity of temperature profiles in distant galaxy clusters: the quest for a universal law. *Astronomy&Astrophysics*.

[Balogh et al., 2006] Balogh, M. L., Babul, A., Voit, G. M., McCarthy, I. G., Jones, L. R., Lewis, G. F., and Ebeling, H. (2006). An analytic investigation of the scatter in the integrated x-ray properties of galaxy groups and clusters. *Monthly Notices of the Royal Astronomical Society*, 366(2):624–634.

[Barnes et al., 2017] Barnes, D. J., Vogelsberger, M., Kannan, R., Marinacci, F., Weinberger, R., Springel, V., Torrey, P., Pillepich, A., Nelson, D., Pakmor, R., Naiman, J., Hernquist, L., and McDonald, M. (2017). A census of cool core galaxy clusters in illustristng.

[Biffi et al., 2012] Biffi, V., Dolag, K., and Boehringer, H. (2012). Investigating the velocity structure and x-ray observable properties of simulated galaxy clusters with phox.

[Biffi et al., 2017] Biffi, V., Planelles, S., Borgani, S., Fabjan, D., Rasia, E., Murante, G., Tornatore, L., Dolag, K., Granato, G. L., Gaspari, M., and Beck, A. M. (2017). The history of chemical enrichment in the intracluster medium from cosmological simulations.

[Boehringer et al., 2011] Boehringer, H., Dolag, K., and Chon, G. (2011). On the self-similar appearance of galaxy clusters in x-rays.

[Boehringer et al., 2010] Boehringer, H., Pratt, G. W., Arnaud, M., Borgani, S., Croston, J. H., Ponman, T. J., Ameglio, S., Temple, R. F., and Dolag, K. (2010). Substructure of the galaxy clusters in the REXCESS sample: observed statistics and comparison to numerical simulations. *Astronomy and Astrophysics*, 514:A32.

[Boerner, 1995] Boerner, G. (1995). *The Early Universe: Facts and Fiction (Theoretical and Mathematical Physics)*. Springer.

[Burns et al., 2008] Burns, J. O., Hallman, E. J., Gantner, B., Motl, P. M., and Norman, M. L. (2008). Why do only some galaxy clusters have cool cores? *The Astrophysical Journal*, 675(2):1125–1140.

[Churazov et al., 2005] Churazov, E., Sazonov, S., Sunyaev, R., Forman, W., Jones, C., and Bhringer, H. (2005). Supermassive black holes in elliptical galaxies: Switching from very bright to very dim. In *ESO Astrophysics Symposia*, pages 295–299. Springer Berlin Heidelberg.

[Dennis and Chandran, 2005] Dennis, T. J. and Chandran, B. D. G. (2005). Turbulent heating of galaxy-cluster plasmas. *The Astrophysical Journal*, 622(1):205–216.

[Dolag et al., 2009] Dolag, K., Borgani, S., Murante, G., and Springel, V. (2009). Substructures in hydrodynamical cluster simulations. *Monthly Notices of the Royal Astronomical Society*, 399(2):497–514.

[Dolag et al., 2008] Dolag, K., Bykov, A. M., and Diaferio, A. (2008). Non-thermal processes in cosmological simulations.

[Donahue et al., 2006] Donahue, M., Horner, D. J., Cavagnolo, K. W., and Voit, G. M. (2006). Entropy profiles in the cores of cooling flow clusters of galaxies. *The Astrophysical Journal*, 643(2):730–750.

[Dubois et al., 2011] Dubois, Y., Devriendt, J., Teyssier, R., and Slyz, A. (2011). How agn feedback and metal cooling shape cluster entropy profiles.

[Edge, 2001] Edge, A. (2001). The detection of molecular gas in the central galaxies of cooling flow clusters. *Monthly Notices of the Royal Astronomical Society*, 328(3):762–782.

[Fabian, 1994] Fabian, A. C. (1994). Cooling flows in clusters of galaxies. *Annual Review of Astronomy and Astrophysics*, 32(1):277–318.

[Fabjan et al.,] Fabjan, D., Borgani, S., Tornatore, L., Saro, A., Murante, G., and Dolag, K. Simulating the effect of agn feedback on the metal enrichment of galaxy clusters.

[Guo and Oh, 2009] Guo, F. and Oh, S. P. (2009). Could agn outbursts transform cool core clusters?

[Ha et al., 2017] Ha, J.-H., Ryu, D., and Kang, H. (2017). Properties of merger shocks in merging galaxy clusters.

[Hahn et al., 2015] Hahn, O., Martizzi, D., Wu, H.-Y., Evrard, A. E., Teyssier, R., and Wechsler, R. H. (2015). Rhapsody-g simulations i: the cool cores, hot gas and stellar content of massive galaxy clusters.

[Henning et al., 2009] Henning, J. W., Gantner, B., Burns, J. O., and Hallman, E. J. (2009). ON THE ORIGIN OF COOL CORE GALAXY CLUSTERS: COMPARING x-RAY OBSERVATIONS WITH NUMERICAL SIMULATIONS. *The Astrophysical Journal*, 697(2):1597–1620.

[Henriksen and Mushotzky, 1986] Henriksen, M. J. and Mushotzky, R. F. (1986). The x-ray spectrum of the coma cluster of galaxies. *The Astrophysical Journal*, 302:287.

[Hudson et al., 2009] Hudson, D. S., Mittal, R., Reiprich, T. H., Nulsen, P. E. J., Andernach, H., and Sarazin, C. L. (2009). What is a cool-core cluster? a detailed analysis of the cores of the x-ray flux-limited hiflugcs cluster sample. *Astronomy&Astrophysics*.

[Johnson et al., 2009] Johnson, R., Ponman, T. J., and Finoguenov, A. (2009). A statistical analysis of the two-DimensionalXMM-NewtonGroup survey: the impact of feedback on group properties. *Monthly Notices of the Royal Astronomical Society*, 395(3):1287–1308.

[Kay et al., 2007] Kay, S. T., Silva, A. C. D., Aghanim, N., Blanchard, A., Liddle, A. R., Puget, J.-L., Sadat, R., and Thomas, P. A. (2007). The evolution of clusters in the CLEF cosmological simulation: X-ray structural and scaling properties. *Monthly Notices of the Royal Astronomical Society*, 377(1):317–334.

[Komatsu et al., 2011] Komatsu, E., Smith, K. M., Dunkley, J., Bennett, C. L., Gold, B., Hinshaw, G., Jarosik, N., Larson, D., Nolta, M. R., Page, L., Spergel, D. N., Halpern, M., Hill, R. S., Kogut, A., Limon, M., Meyer, S. S., Odegard, N., Tucker, G. S., Weiland, J. L., Wollack, E., and Wright, E. L. (2011). SEVEN-YEARWILKINSON MICROWAVE ANISOTROPY PROBE(WMAP) OBSERVATIONS: COSMOLOGICAL INTERPRETATION. *The Astrophysical Journal Supplement Series*, 192(2):18.

[Kravtsov and Borgani, 2012] Kravtsov, A. and Borgani, S. (2012). Formation of galaxy clusters.

[Landry et al., 2012] Landry, D., Bonamente, M., Giles, P., Maughan, B., and Joy, M. (2012). Chandra measurements of a complete sample of x-ray luminous galaxy clusters: the gas mass fraction.

[McCarthy et al., 2008] McCarthy, I. G., Babul, A., Bower, R. G., and Balogh, M. L. (2008). Towards a holistic view of the heating and cooling of the intracluster medium. *Monthly Notices of the Royal Astronomical Society*, 386(3):1309–1331.

[McCarthy et al., 2004] McCarthy, I. G., Balogh, M. L., Babul, A., Poole, G. B., and Horner, D. J. (2004). Models of the intracluster medium with heating and cooling: Explaining the global and structural x-ray properties of clusters. *The Astrophysical Journal*, 613(2):811–830.

[McDonald et al., 2013] McDonald, M., Benson, B. A., Vikhlinin, A., Stalder, B., Bleem, L. E., Lin, H. W., Aird, K. A., Ashby, M. L. N., Bautz, M. W., Bayliss, M., Bocquet, S., Brodwin, M., Carlstrom, J. E., Chang, C. L., Cho, H. M., Clocchiatti, A., Crawford, T. M., Crites, A. T., de Haan, T., Desai, S., Dobbs, M. A., Dudley, J. P., Foley, R. J., Forman, W. R., George, E. M., Gettings, D., Gladders, M. D., Gonzalez, A. H., Halverson, N. W., High, F. W., Holder, G. P., Holzapfel, W. L., Hoover, S., Hrubes, J. D., Jones, C., Joy, M., Keisler, R., Knox, L., Lee, A. T., Leitch, E. M., Liu, J., Lueker, M., Luong-Van, D., Mantz, A., Marrone, D. P., McMahon, J. J., Mehl, J., Meyer, S. S., Miller, E. D., Mocanu, L., Mohr, J. J., Montroy, T. E., Murray, S. S., Nurgaliev, D., Padin, S., Plagge, T., Pryke, C., Reichardt, C. L., Rest, A., Ruel, J., Ruhl, J. E., Saliwanchik, B. R., Saro, A., Sayre, J. T., Schaffer, K. K., Shirokoff, E., Song, J., Suhada, R., Spieler, H. G., Stanford, S. A., Staniszewski, Z., Stark, A. A., Story, K., van Engelen, A., Vanderlinde, K., Vieira, J. D., Williamson, R., Zahn, O., and Zenteno, A. (2013). The growth of cool cores and evolution of cooling properties in a sample of 83 galaxy clusters at 0.3 ¡ z ¡ 1.2 selected from the spt-sz survey.

[McNamara, 2004] McNamara, B. R. (2004). Star formation in cluster cooling flows.

[McNamara and OConnell, 1989] McNamara, B. R. and OConnell, R. W. (1989). Star formation in cooling flows in clusters of galaxies. *The Astronomical Journal*, 98:2018.

[Molendi and Pizzolato, 2001] Molendi, S. and Pizzolato, F. (2001). Is the gas in cooling flows multiphase? *The Astrophysical Journal*, 560(1):194–200.

[Nagai and Dolag, prep] Nagai, D. and Dolag, K. (in prep).

[O'Hara et al., 2006] O'Hara, T. B., Mohr, J. J., Bialek, J. J., and Evrard, A. E. (2006). Effects of mergers and core structure on the bulk properties of nearby galaxy clusters. *The Astrophysical Journal*, 639(1):64–80.

[Peterson et al., 2003] Peterson, J. R., Kahn, S. M., Paerels, F. B. S., Kaastra, J. S., Tamura, T., Bleeker, J. A. M., Ferrigno, C., and Jernigan, J. G. (2003). High-resolution x-ray spectroscopic constraints on cooling-flow models for clusters of galaxies. *The Astrophysical Journal*, 590(1):207–224.

[Poole et al., 2008] Poole, G. B., Babul, A., McCarthy, I. G., Sanderson, A. J. R., and Fardal, M. A. (2008). The impact of mergers on relaxed x-ray clusters - III. effects on compact cool cores. *Monthly Notices of the Royal Astronomical Society*, 391(3):1163–1175.

[Pratt et al., 2009] Pratt, G. W., Arnaud, M., Piffaretti, R., Boehringer, H., Ponman, T. J., Croston, J. H., Voit, G. M., Borgani, S., and Bower, R. G. (2009). Gas entropy in a representative sample of nearby x-ray galaxy clusters (rexcess): relationship to gas mass fraction.

[Rasia et al., 2015] Rasia, E., Borgani, S., Murante, G., Planelles, S., Beck, A. M., Biffi, V., Ragone-Figueroa, C., Granato, G. L., Steinborn, L. K., and Dolag, K. (2015). Cool core clusters from cosmological simulations.

[Rossetti et al., 2017] Rossetti, M., Gastaldello, F., Eckert, D., Torre, M. D., Pantiri, G., Cazzoletti, P., and Molendi, S. (2017). The cool core state of planck sz-selected clusters versus x-ray selected samples: evidence for cool core bias.

[Rossetti and Molendi, 2010] Rossetti, M. and Molendi, S. (2010). Cool core remnants in galaxy clusters. *Astronomy and Astrophysics*, 510:A83.

[Ruszkowski and Begelman, 2002] Ruszkowski, M. and Begelman, M. C. (2002). Heating, conduction, and minimum temperatures in cooling flows. *The Astrophysical Journal*, 581(1):223–228.

[Ruszkowski et al., 2004] Ruszkowski, M., Bruggen, M., and Begelman, M. C. (2004). Cluster heating by viscous dissipation of sound waves. *The Astrophysical Journal*, 611(1):158–163.

[Sanders et al., 2008] Sanders, J. S., Fabian, A. C., Allen, S. W., Morris, R. G., Graham, J., and Johnstone, R. M. (2008). Cool x-ray emitting gas in the core of the centaurus cluster of galaxies. *Monthly Notices of the Royal Astronomical Society*, 385(3):1186–1200.

[Sanderson et al., 2009a] Sanderson, A. J. R., Edge, A. C., and Smith, G. P. (2009a). LoCuSS: the connection between brightest cluster galaxy activity, gas cooling and dynamical disturbance of x-ray cluster cores. *Monthly Notices of the Royal Astronomical Society*, 398(4):1698–1705.

[Sanderson et al., 2009b] Sanderson, A. J. R., O'Sullivan, E., Ponman, T. J., and) (2009b). A statistically-selected chandra sample of 20 galaxy clusters – ii. gas properties and cool-core/non-cool core bimodality.

[Sanderson et al., 2006] Sanderson, A. J. R., Ponman, T. J., and O'Sullivan, E. (2006). A statistically-selected chandra sample of 20 galaxy clusters – i. temperature and cooling time profiles.

[Santos et al., 2008] Santos, J. S., Rosati, P., Tozzi, P., Boehringer, H., Ettori, S., and Bignamini, A. (2008). Searching for cool core clusters at high redshift. *Astronomy & Astrophysics*, 483(1):35–47.

[Sarazin, 2009] Sarazin, C. L. (2009). *X-Ray Emission from Clusters of Galaxies*. CAMBRIDGE UNIV PR.

[Schneider, 2008] Schneider, P. (2008). *Einfuehrung in die Extragalaktische Astronomie und Kosmologie*. Springer-Verlag GmbH.

[Simionescu et al., 2015] Simionescu, A., Werner, N., Urban, O., Allen, S. W., Ichinohe, Y., and Zhuravleva, I. (2015). A uniform contribution of core-collapse and type ia supernovae to the chemical enrichment pattern in the outskirts of the virgo cluster.

[Smith et al., 2005] Smith, G. P., Kneib, J.-P., Smail, I., Mazzotta, P., Ebeling, H., and Czoske, O. (2005). A hubble space telescope lensing survey of x-ray luminous galaxy clusters - IV. mass, structure and thermodynamics of cluster cores at z = 0.2. *Monthly Notices of the Royal Astronomical Society*, 359(2):417–446.

[Springel, 2005] Springel, V. (2005). *User guide for GADGET-2*.

[Springel et al., 2000] Springel, V., White, S., Tormen, G., and Kauffmann, G. (2000). Populating a cluster of galaxies - i. results at z=0.

[Valenti, 2013] Valenti, R. (2013). Thermodynamics and statistical physics. Technical report, Institut fuer Theoretische Physik Universitaet Frankfurt.

[Vikhlinin et al., 2006] Vikhlinin, A., Burenin, R., Forman, W. R., Jones, C., Hornstrup, A., Murray, S. S., and Quintana, H. (2006). Lack of cooling flow clusters at z¿0.5.

[Vikhlinin et al., 2005] Vikhlinin, A., Kravtsov, A., Forman, W., Jones, C., Markevitch, M., Murray, S. S., and Speybroeck, L. V. (2005). Chandra sample of nearby relaxed galaxy clusters: mass, gas fraction, and mass-temperature relation.

[Voit et al., 2005] Voit, G. M., Kay, S. T., and Bryan, G. L. (2005). The baseline intra-cluster entropy profile from gravitational structure formation. *Monthly Notices of the Royal Astronomical Society*, 364(3):909–916.

List of Figures

List of Tables

A Derivations and Explanations

A.1 Differentiation and Transformation of the Hydrostatic Equilibrium Equation

In Sect. 2.1.2 the equation of the hydrostatic equilibrium in spherical coordinates, Eq. (2.4) is differentiated with respect to r and then some transformations are done to achieve Eq. (2.5). For these transformations another equation is necessary that gives the correlation of mass and mass density:

$$M(r) = 4\pi \int_0^r dr' r'^2 \rho(r'). \tag{A.1}$$

In the first step Eq. (2.4) is differentiated with respect to r:

$$\frac{d}{dr}\frac{dP}{dr} = -\frac{GM}{r^2}\frac{d\rho}{dr} - \frac{G\rho}{r^2}\frac{dM}{dr} - \rho GM\frac{dr^{-2}}{dr}. \tag{A.2}$$

Then, this term is transformed and Eq. (A.1) is inserted:

$$\begin{aligned} \frac{d}{dr}\frac{dP}{dr} &= -\frac{GM}{r^2}\frac{d\rho}{dr} - \frac{G\rho}{r^2}4\pi r^2\rho + \frac{2\rho GM}{r^3}, \\ \frac{d}{dr}\frac{dP}{dr} &+ \frac{GM}{r^2}\frac{d\rho}{dr} + 4\pi G\rho^2 - \frac{2\rho GM}{r^3} = 0, \\ \frac{r^2}{\rho}\frac{d}{dr}\frac{dP}{dr} &+ \frac{GM}{\rho}\frac{d\rho}{dr} + 4\pi G r^2\rho - \frac{2GM}{r} = 0. \end{aligned} \tag{A.3}$$

Subsequently, equ. 2.4 is inserted into the second and last term:

$$\begin{aligned} \frac{r^2}{\rho}\frac{d}{dr}\frac{dP}{dr} - \frac{r^2}{\rho^2}\frac{dP}{dr}\frac{d\rho}{dr} + 4\pi G r^2\rho - \frac{2r}{\rho}\frac{dP}{dr} &= 0, \\ \frac{r^2}{\rho}\frac{d}{dr}\frac{dP}{dr} - \frac{r^2}{\rho^2}\frac{dP}{dr}\frac{d\rho}{dr} - \frac{2r}{\rho}\frac{dP}{dr} + 4\pi G r^2\rho &= 0. \end{aligned} \tag{A.4}$$

Finally, the three first terms can be summarized and Eq. (2.5) is found:

$$\frac{d}{dr}\left(\frac{r^2}{\rho}\frac{dP}{dr}\right) + 4\pi G r^2\rho = 0. \tag{A.5}$$

A.2 Entropy Derivation

In Sect. 2.1.4 the entropy as a measure for the thermodynamical properties of the ICM is introduced. Eq. (2.25) is the astronomical entropy which is propertional to the thermodynamical entropy. The following paragraph derives the thermodynamical entropy from statistical physics and presents the relation of thermodynamical and astrophysical entropy. In statistical physics, the canonical partition function of an ideal gas is given by (e.g. see [Valenti, 2013]):

$$Z_N(T,V) = \frac{1}{N!}\left(\frac{V}{\lambda_T^3}\right)^N, \tag{A.6}$$

with the thermal wavelength $\lambda_T = \frac{h}{\sqrt{2\pi m k_B T}}$. Here from, the free energy F can be deduced [Valenti, 2013]:

$$\begin{aligned} F(T,V,N) &= -k_B T \ln\left(\frac{1}{N!}\left(\frac{V}{\lambda_T^3}\right)^N\right), \\ &= -k_B T \left(\ln\left(\frac{1}{N!}\right) + N\ln\left(\frac{V}{\lambda_T^3}\right)\right), \\ &= -k_B T \left(-N\ln(N) + N + N\ln\left(\frac{V}{\lambda_T^3}\right)\right), \\ &= -N k_B T \left(\ln\left(\frac{V}{N\lambda_T^3}\right) + 1\right). \end{aligned} \tag{A.7}$$

Finally, the entropy S can be calculated by building the partial derivative of the free energy from T [Valenti, 2013]:

$$\begin{aligned} S &= -\left(\frac{\partial F}{\partial T}\right)|_{V,N} = N k_B \left(\ln\left(\frac{V}{N\lambda_T^3}\right) + 1\right) - \frac{\partial}{\partial T}\left(N k_B T \left(\ln\left(\frac{N\lambda_T^3}{V}\right) - 1\right)\right), \\ &= N k_B \left(\ln\left(\frac{V}{N\lambda_T^3}\right) + 1\right) - N k_B T \left(\frac{V}{\lambda_T^3}\cdot\frac{N}{V}\lambda_T^2\cdot\frac{-3}{2}\cdot\frac{\lambda_T}{T}\right), \\ &= N k_B \left(\ln\left(\frac{V}{N\lambda_T^3}\right) + \frac{5}{2}\right), \\ &= N k_B \left(\ln\left(\frac{V(2\pi m k_B T)^{3/2}}{N h^3}\right) + \frac{5}{2}\right). \end{aligned} \tag{A.8}$$

This formula is also known as Sackur-Tetrode equation. The entropy used in cluster researches refers only to a part of this real thermodynamic entropy. A new entropy K is introduced which can be easily calculated with values that can be measured from observations. K is proportional to S in the sense of:

$$S = k_B \ln(K^{3/2}) + S_0. \tag{A.9}$$

Therefore, K is:

$$\begin{aligned} K^{3/2} &= \frac{V(2\pi m k_B T)^{3/2}}{N h^3}, \\ &= \frac{2\pi m {k_B}^{3/2}}{h^3} \frac{V}{N} T^{3/2}, \\ &= \left(\frac{2\pi m k_B h^{-2}}{h^3} \left(\frac{V}{N} \right)^{2/3} T \right)^{3/2}, \\ &= \left(\frac{2\pi m k_B h^{-2}}{h^3} n^{-2/3} T \right)^{3/2}. \end{aligned} \tag{A.10}$$

As K should only be proportional to the real thermodynamic entropy, the new entropy is defined as $K = n^{-2/3}T$. The number density and temperature of clusters can be derived from the emissivity of the clusters and therefore the entropy K can be determined.

A.3 Sunyaev-Zel'dovich Effect

The Sunyaev-Zel'dovich effect is based on the inverse Compton scattering of CMB photons with electrons from the ICM. If a low-energy photon from the CMB scatters with an high-energy electron from the hot plasma of the ICM, its wavelength decreases which means its energy increases. The scatter process can lead to a deflection of an electron that would have been in the line of sight with the observer. Applying statistics, it can be assumed that another electron that was not in the line of sight with observer will also be scatter and will thereby is deflected into the observer's direction. This assumption can be made because the CMB is istropically distributed. The scattered photons that reach the observer have a higher energy spectrum than the CMB photons. This difference in the spectra can be used to idenfiy clusters and position. Further examinations can also determine properties such as density and temperature of these clusters. [Schneider, 2008]

A.4 Derivation of the T-M Scaling Relation

The basic assumption for deriving scaling relations is that the evolution of the baryonic matter is dominated by the dark matter evolution. In the hierarchical structure model, the matter collapse due to gravitational forces and begin to built structures starting from a density distribution with very small deviations. Coming along with the gravitational collapse, dense regions condense further and further building regions of overdensities. Thus, the mass of collapsed structures such as clusters can be defined using a spherical overdensity that is set into relation to a reference density. In the cosmological context, the most commonly used reference density is the critical density that corresponds with the density

of a flat universe. A mass in this condition would be defined as

$$M_\Delta = \frac{4\pi}{3}\Delta\rho_{crit}(z)R_\Delta^3, \tag{A.11}$$

with R_Δ being the radius within which the mass is calculated, Δ being the overdensity value and $\rho_{crit} = \frac{3H_0^2E^2(z)}{8\pi G}$. If only gravitational forces act on the matter, the main parameter that determines the other properties of the structures is the mass. The clusters collapse in a self-similar way which means that they are scaled versions of each other only differing in mass and size. Following this, the temperature is proportional to radius and mass:

$$T \propto \frac{M}{R}, \tag{A.12}$$

with M being the mass within radius R and T being the temperature at R. Rearranging Equ. A.11 for R and inserting it into Equ. A.12 then results in:

$$T \propto \left(E(z)M_\Delta\right)^{2/3}. \tag{A.13}$$

This equation is referred to as T-M scaling relation. Basically, observed and simulated clusters should follow this equation. Deviations can be explained if hydrodynamical effects are included that would change the power ratio dependence of the quantities. [Boehringer et al., 2011], [Nagai and Dolag, prep]

B Additional Figures

B.1 Central Electron Number Density versus Central Temperature Drop

Fig. B.1 and B.2 show the correlation of the central electron number density versus the central temperature drop of 1199 simulated haloes. Circles refer to haloes that were classified as high-mass haloes, squares correspond to intermediate-mass haloes and diamonds are low-mass haloes. All halos are color-coded according to their mass-weighted median central temperature. In addition, Fig. B.2 is also subdivided into three panels from top to bottom showing high- to low-mass halos. The limit values for all quantities are indicated by the vertical and horizontal dotted lines.

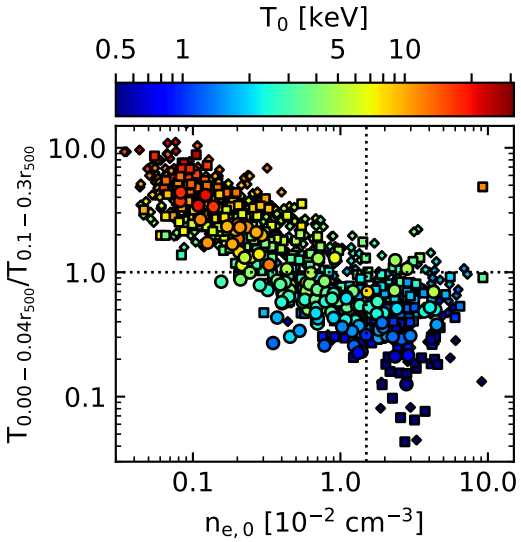

Figure B.1: Correlation of the central electron number density versus the central temperature drop of 1199 simulated haloes. The haloes are color-coded by their central temperature. The sample is subdivided into high-mass haloes (circles), intermediate-mass haloes (squares) and low-mass haloes (diamonds). The vertical and horizontal dotted lines represent thresholds on the quantities which segregate the sample into CC and NCC cluster. $n_{e,0}$ is the mass-weighted median value of the ICM particles within a region of $0.00 - 0.04\ r_{500}$. The central temperature drop is calculated by dividing the mass-weighted median temperature of the inner region ($0.00 - 0.04\ r_{500}$) by the mass-weighted median temperature of the outer region ($0.10 - 0.30\ r_{500}$).

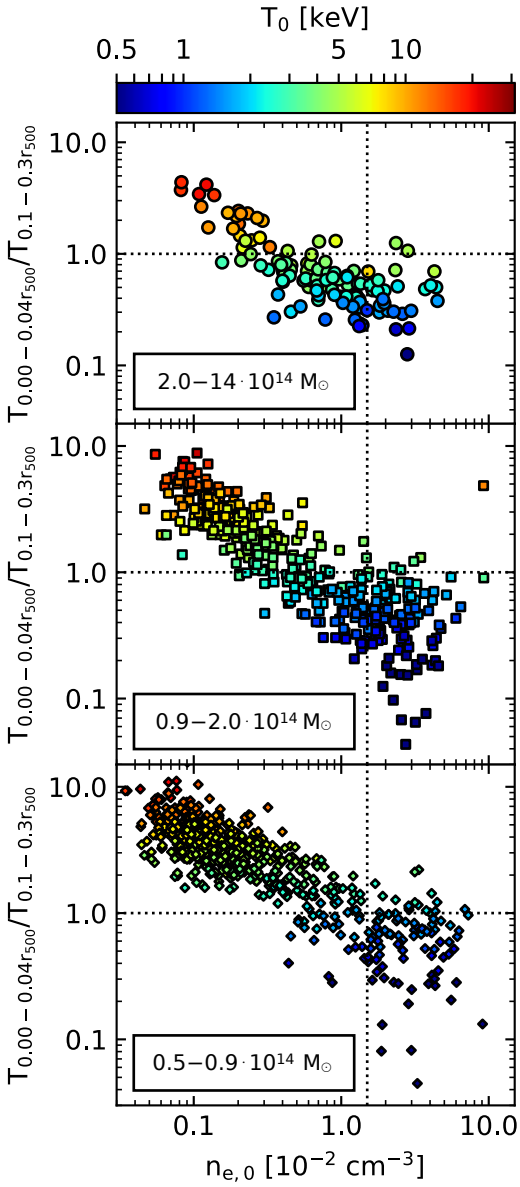

Figure B.2: Correlation of the central electron number density versus the central temperature drop of 1199 simulated haloes. The haloes are color-coded by their central temperature. The top panel shows the high-mass halo sample (circles), the middle one corresponds to the intermediate-mass haloes (squares) and the bottom one includes all low-mass haloes (diamonds). The vertical and horizontal dotted lines represent thresholds on the quantities which segregate the sample into CC and NCC cluster. $n_{e,0}$ is the mass-weighted median value of the ICM particles within a region of $0.00 - 0.04\ r_{500}$. The central temperature drop is calculated by dividing the mass-weighted median temperature of the inner region ($0.00 - 0.04\ r_{500}$) by the mass-weighted median temperature of the outer region ($0.10 - 0.30\ r_{500}$).

B.2 Coolcoreness from Central Cooling Time Versus Central Entropy

Fig. B.3 presents the same plot as the left panel of Fig. 3.1. In addition, the best fitting regression line of all haloes is plotted as black line. The blue points with red vertical lines indicate the starting and ending points from which the coolcoreness of the haloes is determined. Haloes below the start point are assigned a coolcoreness of 0%. Haloes above the ending point are defined to have a coolcoreness of 100%.

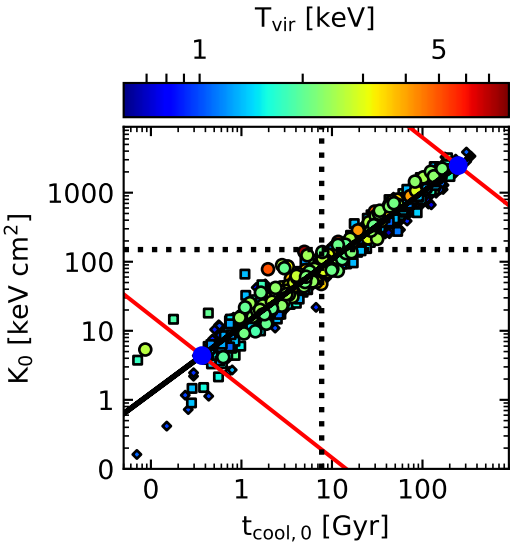

Figure B.3: Correlation of the central cooling time versus the central entropy of 1199 simulated haloes. The haloes are color-coded by their virial temperature. The sample is subdivided into high-mass haloes (circles), intermediate-mass haloes (squares) and low-mass haloes (diamonds). The vertical and horizontal dotted lines represent thresholds on the quantities which segregate the sample into CC and NCC cluster. K_0 and $t_{cool,0}$ are the mass-weighted median values of the ICM particles within a region of $0.00 - 0.04\ r_{500}$. The black line is the regression line fit in log-log scale on the plot through all haloes. The blue points with vertical red lines indicate the starting and ending point from which the coolcoreness of the haloes is determined.

Danksagung

An dieser Stelle möchte ich mich bei allen Personen bedanken, die durch ihre fachliche und persönliche Unterstützung zum Gelingen dieser Bachelorarbeit beigetragen haben.
Mein grösster Dank gilt meinem Betreuer Dr. Klaus Dolag, der dieses interessante Thema bereitgestellt hat, mir bei Fragen jeglicher Art jederzeit zur Verfügung stand und mich stets mit neuen Ideen und Ansätzen inspiriert hat.
Weiterhin möchte ich Frau Lisa Steinborn danken, die mich besonders bei der Einarbeitung in die Simulation sowie all den Kleinigkeiten und Fragen, die während meiner Arbeit anfielen, unterstützt hat.
Zudem danke ich Dr. Tadziu Hoffmann für seine Hilfe bei der Erstellung der Median Kurven der Gas Fraction Plots.
Zuletzt auch noch ein herzliches Dankeschön an Martin Denk, Dr. Christian Obermeier und Ludwig Böss für die Korrektur meiner Arbeit, die äusserst nützlichen Anmerkungen und die konstruktive Kritik.

Selbständigkeitserklärung

Hiermit erkläre ich, dass ich die vorliegende Arbeit eigenständig und ohne fremde Hilfe angefertigt habe. Textpassagen, die wörtlich oder dem Sinn nach auf Publikationen oder Vorträgen anderer Autoren beruhen, sind als solche kenntlich gemacht. Die Arbeit wurde bisher keiner anderen Prüfungsbehörde vorgelegt und auch noch nicht veröffentlicht.

Ort, Datum	Jennifer Hinz